Monthly Notices
of the
ROYAL ASTRONOMICAL SOCIETY

MNRAS **458,** 1742–1767 (2016)
Advance Access publication 2016 February 23

doi:10.1093/mnras/stw359

Submillimeter array observations of NGC 2264-C: molecular outflows and driving sources

Nichol Cunningham,[1,2]★ Stuart L. Lumsden,[1] Claudia J. Cyganowski,[3,4] Luke T. Maud[1,5] and Cormac Purcell[6]

[1]*School of Physics and Astronomy, University of Leeds, Leeds LS2 9JT, UK*
[2]*National Radio Astronomy Observatory, PO Box 2, Green Bank, WV 24944, USA*
[3]*Scottish Universities Physics Alliance (SUPA), School of Physics and Astronomy, University of St Andrews, St Andrews, Fife KY16 9SS, UK*
[4]*Harvard–Smithsonian Center for Astrophysics, Cambridge, MA 02138, USA*
[5]*Leiden Observatory, Leiden University, PO Box 9513, NL-2300 RA Leiden, the Netherlands*
[6]*Sydney Institute for Astronomy, University of Sydney, NSW 2006, Australia*

Accepted 2016 February 12. Received 2016 February 11; in original form 2014 October 17

ABSTRACT

We present 1.3 mm Submillimeter Array (SMA) observations at ∼3 arcsec resolution towards the brightest section of the intermediate/massive star-forming cluster NGC 2264-C. The millimetre continuum emission reveals ten 1.3 mm continuum peaks, of which four are new detections. The observed frequency range includes the known molecular jet/outflow tracer SiO (5−4), thus providing the first high-resolution observations of SiO towards NGC 2264-C. We also detect molecular lines of 12 additional species towards this region, including CH_3CN, CH_3OH, SO, H_2CO, DCN, HC_3N, and ^{12}CO. The SiO (5−4) emission reveals the presence of two collimated, high-velocity (up to 30 km s^{-1} with respect to the systemic velocity) bipolar outflows in NGC 2264-C. In addition, the outflows are traced by emission from ^{12}CO, SO, H_2CO, and CH_3OH. We find an evolutionary spread between cores residing in the same parent cloud. The two unambiguous outflows are driven by the brightest mm continuum cores, which are IR-dark, molecular line weak, and likely the youngest cores in the region. Furthermore, towards the Red *MSX* Source AFGL 989-IRS1, the IR-bright and most evolved source in NGC 2264-C, we observe no molecular outflow emission. A molecular line rich ridge feature, with no obvious directly associated continuum source, lies on the edge of a low-density cavity and may be formed from a wind driven by AFGL 989-IRS1. In addition, 229 GHz class I maser emission is detected towards this feature.

Key words: stars: formation – ISM: jets and outflows – ISM: molecules.

1 INTRODUCTION

Can high-mass star formation be described as a scaled-up version of low-mass star formation? Protostellar jets and outflows are a ubiquitous feature of the star formation process; as such, their study provides an important means of addressing this fundamental question. Observationally, young stellar objects (YSOs) of all masses are known to drive bipolar molecular outflows. If a single driving mechanism operates in both the low- and high-mass regimes (e.g. Richer et al. 2000), this would be evidence for a common formation process. The initial evidence for a single mechanism was an observed correlation, over five orders of magnitude, between bolometric luminosity and outflow force, power and mass flow rate (e.g. Cabrit & Bertout 1992; Shepherd & Churchwell 1996). Outflows observed towards massive young stellar objects (MYSOs) can contain momentum, mass and energy up to a few orders of magnitude larger (e.g. Beuther et al. 2002; Wu et al. 2004; Zhang et al. 2005) than outflows observed towards lower mass YSOs (e.g. Kim & Kurtz 2006).

A single outflow mechanism would imply that all stars acquire mass by a similar disc-accretion process that scales with source luminosity. However, outflows observed towards MYSOs were initially suggested to be less collimated than those identified towards low-mass YSOs (e.g. Wu et al. 2004). In contrast, both Beuther et al. (2004) and Zhang et al. (2005) identified similar degrees of collimation towards the jets/outflows driven by young MYSOs as found in jets/outflows from low-mass YSOs. To account for both low and high degrees of collimation of massive outflows, Beuther & Shepherd (2005) proposed a scenario in which an initially well-collimated jet/outflow de-collimates with time, eventually forming a wide angle wind. In the early formation stages outflows driven

★E-mail: ncunning@nrao.edu

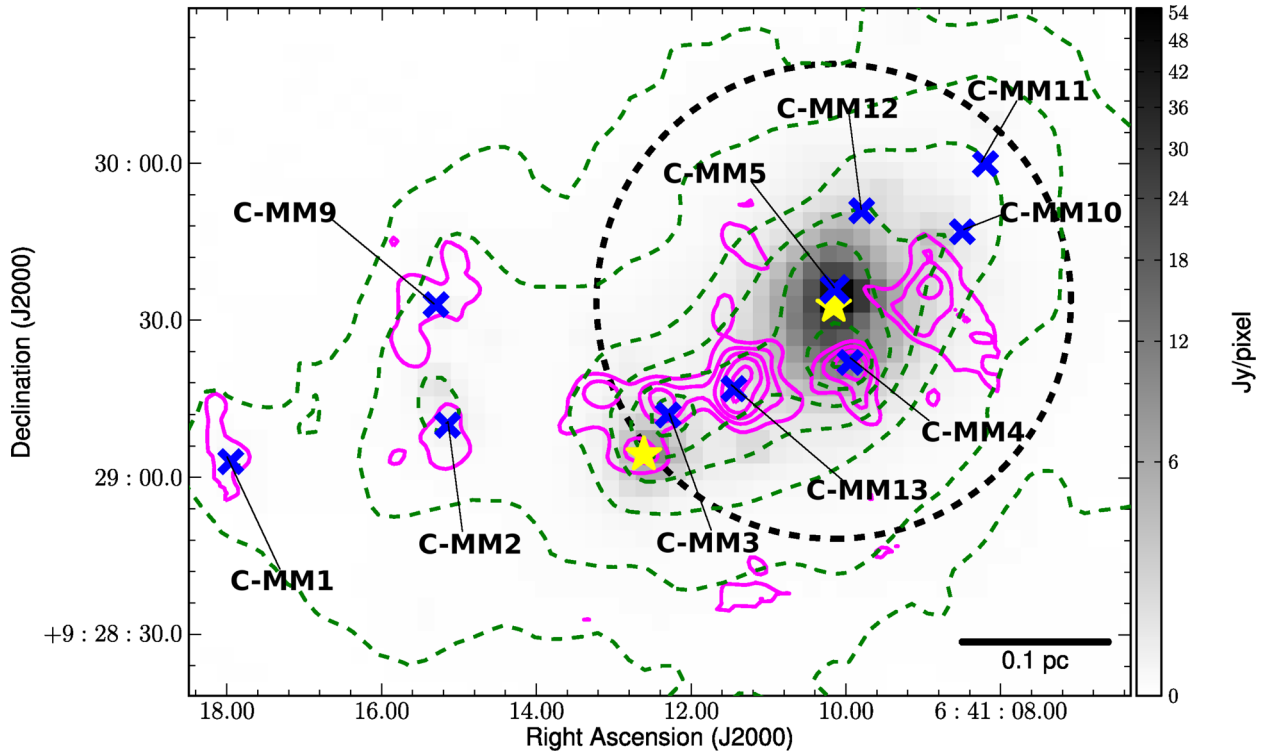

Figure 1. *Herschel* PACS 70 μm emission (grey-scale, the emission is plotted on a log scale) overlaid with contours of SCUBA 450 μm emission (dashed green) and N_2H^+ (1−0) integrated intensity (PdBI, magenta). The N_2H^+ (1−0) integrated intensity map was presented in Peretto et al. (2007) and provided to us by N. Peretto, the contours are the same as given in that paper and are from 1 Jy beam^{-1} to 5 Jy beam^{-1} in steps of 1 Jy beam^{-1}. The SCUBA contours are given by $1\sigma = 0.9$ Jy beam^{-1} × 5,10,20,30,40,50,60. Blue crosses (x) mark the positions of millimetre sources reported by Peretto et al. (2006, 2007); yellow stars mark the positions of the brightest 24 μm *Spitzer* point sources in the region (taken directly from the archive mosaic). The section of NGC 2264-C presented in this work is shown by the dashed black circle which represents the 10 per cent power level of the SMA primary beam centred on RA (J2000) $06^h41^m10\overset{s}{.}13$, Dec. (J2000) $09°29'34\overset{''}{.}0$.

by MYSOs are potentially magnetically dominated and therefore highly collimated (e.g. HH80/81; Carrasco-González et al. 2010). For more evolved MYSOs, a radiatively driven stellar wind naturally gives rise to a less collimated outflow (e.g. Vaidya et al. 2011).

Intermediate-mass YSOs ($2\,M_\odot \leq M_* \leq 8\,M_\odot$) link the low- and high-mass regimes, and so have the potential to provide key insights into whether outflow properties scale smoothly with the mass of the driving (proto)star. A complication is that intermediate and high-mass stars generally form in clustered environments (Lada & Lada 2003); as a result, it is not always unambiguously clear from observations which core(s) in a region are powering the jet/outflow(s), particularly at lower spatial resolution. High angular resolution studies that can resolve individual cores and outflows are thus crucial to understanding jets/outflows from intermediate and high-mass stars.

We targeted NGC 2264-C, one of the nearest intermediate/high-mass star-forming regions in the Red *MSX* Source (RMS) survey (Lumsden et al. 2013), with the Submillimeter Array (SMA). The aim of these observations was to resolve the SiO emission seen with the James Clerk Maxwell Telescope (JCMT, Section 2.2), and so identify which source(s) in the region are driving *active* outflows. A particular goal was to assess the relationship of the RMS source to the outflows seen at low angular resolution, and so to aid in the interpretation of a large, low-resolution outflow survey of RMS objects (Maud et al. 2015).

Located in the Mon OB1 giant molecular cloud complex at a distance of 738^{+57}_{-50} pc (Kamezaki et al. 2014), NGC-2264-C is a comparatively well-studied region, with a wealth of ancillary data and known CO outflows. AFGL 989-IRS1 (Allen 1972), a 9.5 $M_\odot$ B2 star, dominates the region in the IR. 13 millimetre continuum sources have been identified (Ward-Thompson et al. 2000; Peretto, André & Belloche 2006; Peretto, Hennebelle & André 2007, see Fig. 1), which have typical diameters of ∼0.04 pc and masses ranging from ∼2 to 40 $M_\odot$ (Peretto et al. 2006, 2007). From comparing observations and SPH simulations, Peretto et al. (2007) suggest that NGC 2264-C is in a global state of collapse on to the central, most massive millimetre core, C-MM3 (∼40 $M_\odot$). Maury, André & Li (2009) observed ^{12}CO (2−1) emission with the IRAM 30 m (∼11 arcsec resolution), detecting a network of 11 outflow lobes with projected velocities ranging from 10 to 30 km s^{-1}, lengths of 0.2–0.8 pc and momentum fluxes in the range 0.5–50 × 10^{-5} $M_\odot$ km s^{-1} yr^{-1}. However, the limited angular resolution meant that only a small minority of the detected outflow lobes could be unambiguously identified with driving sources (millimetre continuum cores). Subsequent high-resolution SMA observations by Saruwatari et al. (2011) focusing on the central class 0 protostellar core, C-MM3, identified a compact, young north–south bipolar outflow driven by this source in both ^{12}CO and CH_3OH emission, emphasizing the power of high-resolution, multiline observations.

The ambiguity in identifying outflow driving sources based on low-resolution single-dish observations calls for high angular resolution observations of a reliable jet/outflow tracer. Silicon monoxide (SiO) emission is an effective tracer of jets/outflows from both low-mass YSOs (e.g. Gibb et al. 2004; Sakai et al. 2010; Tafalla et al. 2010; López-Sepulcre et al. 2011; Codella et al. 2014) and MYSOs (e.g. Gibb, Davis & Moore 2007; Codella et al. 2013; Leurini et al.

2013; Sánchez-Monge et al. 2013). Importantly, SiO emission, unlike CO, does not suffer from confusion with easily excited ambient material. CO emission can also be easily excited in outflows, which may obscure the underlying effects; it is possible for weak outflows to effectively be 'fossil' momentum-driven remnants even after the central driving engine declines (e.g. Klaassen et al. 2006; Hunter et al. 2008). In contrast, SiO requires the passage of fast shocks to release it into the gas phase (e.g. Gusdorf et al. 2008a; Guillet, Jones & Pineau Des Forêts 2009) and thus is an excellent tracer of the fast shocks associated with an active outflow near the stellar driving source (e.g. Schilke et al. 1997).

We present the first high angular resolution study (∼3 arcsec resolution with the SMA) of SiO (5−4) emission towards NGC 2264-C. The main goals of the SMA observations are to identify *active* outflows and their central driving sources, and to determine the relationship of these active outflows to the multiple outflows previously reported based on single-dish observations of the region. In Section 2, we summarize the observations presented in this paper. We present our results in Section 3, discuss the physical properties of the detected cores and outflows in Section 4, and summarize our conclusions in Section 5.

2 OBSERVATIONS AND DATA REDUCTION

2.1 SMA observations

Our SMA[1] observations were made with eight antennas in the compact configuration on 2010 December 12. The pointing centre for the observations is RA (J2000) $06^{h}41^{m}10\overset{s}{.}13$, Dec. (J2000) $09^{\circ}29'34\overset{''}{.}0$. We observed on-source for a total of ∼4 h, spread over an 8 h track to improve UV coverage. The system temperatures ranged from ∼100 to 180 K depending on source elevation. A typical value of $\tau_{(225\,\mathrm{GHz})}$ ∼0.1–0.15 was obtained during the observations. At 1.3 mm, the SMA primary beam is ∼55 arcsec (FWHP), and the largest recoverable scale for the array in the compact configuration is ∼20 arcsec. The total observed bandwidth is ∼8 GHz, covering ∼216.8–220.8 GHz in the lower sideband and ∼228.8–232.8 GHz in the upper sideband.

Initial calibration was accomplished in MIRIAD (Sault, Teuben & Wright 1995), with further processing undertaken in CASA.[2] The bandpass calibration was derived from observations of the quasar 3C454.3. The gain calibrators were J0530+135, J0532+075, and J0739+016, and the absolute flux calibration was derived from Uranus. The fluxes derived for the quasars were found to be within 20 per cent of the SMA monitoring values, which suggests that the absolute flux calibration is good to within 20 per cent. The upper and lower sidebands were treated individually during calibration. The line and continuum emission were separated using the command *uvcontsub* in CASA: only line-free channels were used to estimate the continuum. Self-calibration was performed on the continuum data in each sideband, with the solutions applied to the line data. The SMA correlator was configured to provide a uniform spectral resolution of 0.8125 MHz; the line data were resampled to a velocity resolution of 1.2 km s^{-1}, then Hanning smoothed.

The continuum data from the lower and upper sidebands were combined to produce the final continuum image. The continuum image and line image cubes were cleaned using a robust weighting of 0.5. This results in a synthesized beam size of ∼3.06 × 2.69 arcsec with a PA of approximately −67 deg for the final 1.3 mm continuum image, which has a 1σ rms noise level of ∼2 mJy beam^{-1}. In the Hanning-smoothed spectral line image cubes, the typical 1σ rms noise (per channel) is ∼40 mJy beam^{-1}. Unless otherwise noted, images displayed in figures have not been corrected for the primary beam response of the SMA. All reported measurements were made from images corrected for the primary beam response.

2.2 JCMT observations

The SiO ($J = 8-7$) line (347.3305 GHz) was observed with the Heterodyne Array Receiver Program (HARP) and autocorrelation spectral imaging system (Buckle et al. 2009) at the James Clerk Maxwell Telescope[3] (JCMT) on 2009 April 26. The SiO ($J = 8-7$) data shown in this paper are part of a larger project (M09AU18), which will be presented elsewhere. A position-switched jiggle chop map with the tracking centred on RA (J2000) $06^{h}41^{m}10\overset{s}{.}10$, Dec. (J2000) $09^{\circ}29'34''$ was made with the HARP array. The array is made up of 16 receiver elements; however, at the time of observing receiver H14 was not operational and is therefore missing from our jiggle map. The reference position for the sky subtractions was RA (J2000) $06^{h}46^{m}35\overset{s}{.}50$, Dec. (J2000) $10^{\circ}10'30''$. The standard pointing check was made before the start of each ∼ 30 min observing block on a point-like spectral line standard, which was also used to check the overall flux scale. At 345 GHz the JCMT has a beam size of ∼15 arcsec and a main beam efficiency η_{mb} of 0.61 (Buckle et al. 2009). During the observations, $\tau_{(225\,\mathrm{GHz})}$ ∼ 0.042. The SiO data were smoothed to a velocity resolution of 1.6 km s^{-1} to improve the signal to noise. A 1σ rms noise level of T_{MB} ∼ 0.04 K was achieved in the final map (totalling 66 min of observation time). The data were processed using STARLINK[4] packages and converted to the main beam temperature scale (T_{MB}).

2.3 Archival data

To complement our SMA and JCMT HARP observations, we utilize archival mid-/far-infrared data. These archival data include PACS (Poglitsch et al. 2010) 70 μm observations (observational ID 1342205056, P.I. F. Motte) taken with the ESA *Herschel Space Observatory*[5] (Pilbratt et al. 2010), *Spitzer* MIPSGAL 24 μm observations (Rieke et al. 2004) and SCUBA 450 μm data (Di Francesco et al. 2008).

The *Herschel* PACS 70 μm and SCUBA 450 μm maps are presented in Fig. 1, overlaid with the positions of the brightest *Spitzer* MIPSGAL 24 μm point sources in our SMA field of view.[6] We have corrected the astrometry for the PACS archival data using the *Spitzer* MIPSGAL 24 μm images, which were calibrated against 2MASS point source positions (Skrutskie et al. 2006).

[1] The SMA is a joint project between the Smithsonian Astrophysical Observatory and the Academia Sinica Institute of Astronomy and Astrophysics and is funded by the Smithsonian Institution and the Academia Sinica.
[2] http://casa.nrao.edu

[3] The JCMT has historically been operated by the Joint Astronomy Centre on behalf of the Science and Technology Facilities Council of the United Kingdom, the National Research Council of Canada and the Netherlands Organization for Scientific Research.
[4] http://starlink.eao.hawaii.edu/starlink
[5] *Herschel* is an ESA space observatory with science instruments provided by European-led Principal Investigator consortia and with important participation from NASA.
[6] The positions were measured directly from the downloaded archive level 2 data, the data are saturated at the position of AFGL989-IRS1.

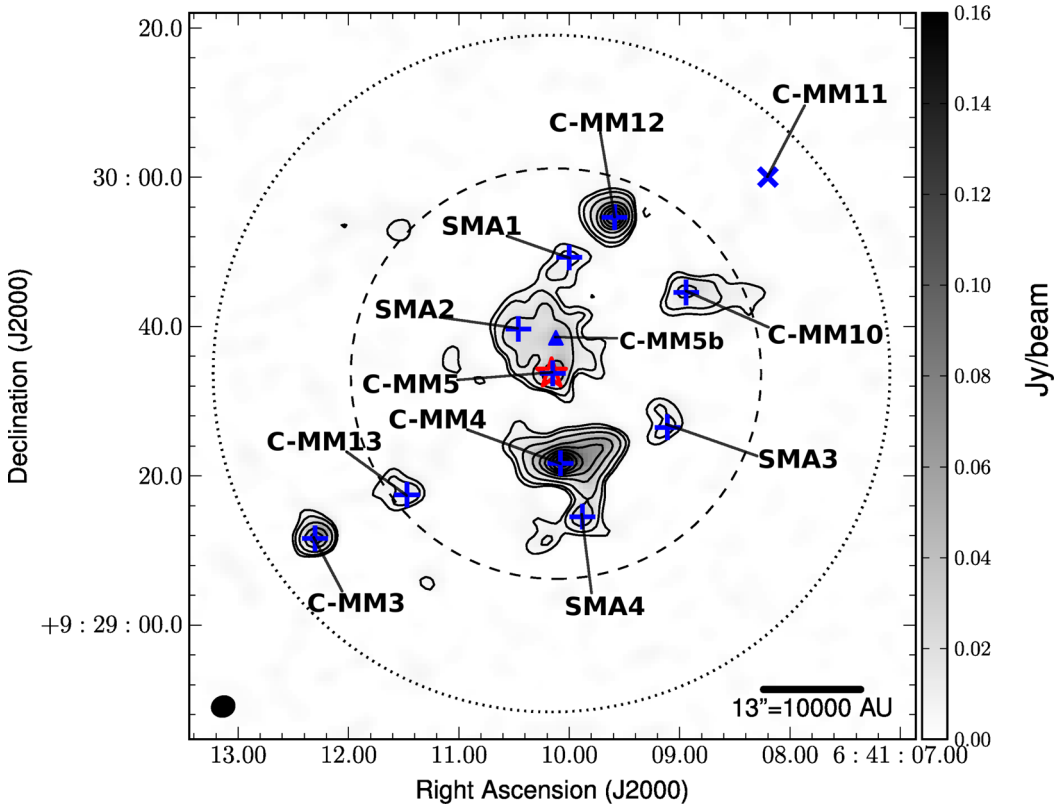

Figure 2. Map of the 1.3 mm continuum emission towards the section of NGC 2264-C observed with the SMA. The grey-scale shows the SMA 1.3 mm continuum emission from 0 to 0.16 Jy beam^{-1}; the peak flux in the field is 0.159 Jy beam^{-1}. The black contours represent (3, 5, 10, 20, 30, 40, 50, 60, 70, 80) $\times$ σ = 2 mJy beam^{-1}. The peak continuum positions for the 10 leaves (millimetre continuum peaks) identified in the dendrogram are marked with blue pluses (+) and labelled SMA – for new detections and C-MM —for previously detected sources. The blue triangle marks the peak position of the possible millimetre continuum peak C-MM5b. The red star represents the position of AFGL 989-IRS1, taken from the 2MASS data in the RMS survey, and the blue cross (x) marks the position of C-MM11 from Peretto et al. (2007). The black dashed circle represents the FWHP of the SMA primary beam, and the outer black dotted circle represents the 10 per cent power level of the SMA primary beam. The SMA synthesized beam (3.06 $\times$ 2.69 arcsec, PA = −69.3) is shown at lower left.

3 RESULTS

3.1 1.3 mm continuum emission

The SMA 1.3 mm continuum image is presented in Fig. 2. The structure of the 1.3 mm emission was characterized through the implementation of dendrograms (Rosolowsky et al. 2008). Dendrograms or structure tree diagrams can be used to define hierarchical structure in clouds. The dendrogram tree structures are comprised of three main components: a trunk, branches and leaves, which correspond to increasing levels of intensity in the data set. We set the minimum threshold intensity required to identify a parent tree structure (e.g. trunk) to be 4σ (in the continuum image prior to correction for the primary beam response; $\sigma \sim 2$ mJy beam^{-1}) and a minimum area of 18 contiguous pixels (the equivalent area of the synthesized beam). Further nested substructures (i.e. branches and leaves) require an additional 1σ increase in intensity, again over a minimum of 18 contiguous pixels. To compute the dendrogram, we have used the PYTHON implementation astrodendro.[7]

We identify 10 millimetre continuum sources in our SMA 1.3 mm image with the dendrogram analysis, of which four are new detections (labelled SMA1-SMA4 in Fig. 2). The other six 1.3 mm continuum sources have been previously reported (Ward-Thompson et al. 2000; Peretto et al. 2006, 2007) and are labelled in Fig. 2 according to the naming scheme of Peretto et al. (C-MM-). Of the ten 1.3 mm continuum sources identified in the dendrogram analysis, five are found as separate, independent parent structures with no substructure, and five are found nested into two tree structures. The two nested structures are comprised of C-MM4 and SMA4, and of C-MM5, SMA1, and SMA2, respectively (see Fig. 3 for an example of nested structure). The parameters of the millimetre continuum sources (e.g. peak intensity, integrated flux density, and effective radius) were extracted using the analysis code *Computing Dendrogram Statistics*[8] and the CASAVIEWER tool, and are presented in Table 1. All properties are estimated from the primary beam corrected 1.3 mm continuum image using a 3σ mask derived from the continuum image prior to correction for the primary beam response. This approach was taken to avoid including noise in the parameter estimates for millimetre continuum sources far from the pointing centre.

We detect all of the previously identified millimetre continuum peaks within the FWHP of our SMA primary beam. Of the sources reported by Peretto et al. (2006) and Peretto et al. (2007) that fall

[7] This research made use of astrodendro, a PYTHON package to compute dendrograms of astronomical data (http://www.dendrograms.org/).

[8] This research made use of Astropy, a community-developed core PYTHON package for astronomy (Astropy Collaboration et al. 2013).

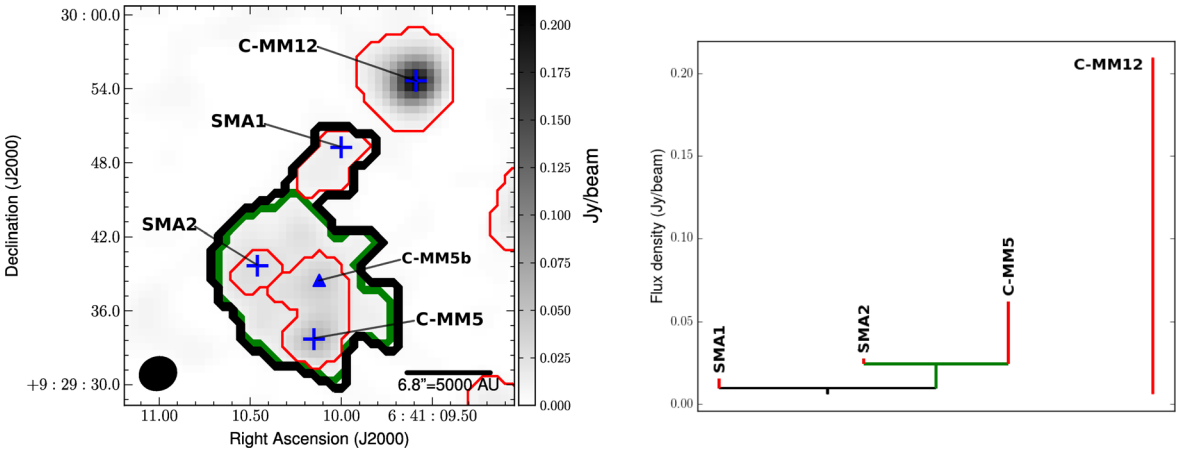

Figure 3. Examples of dendrogram tree structure for C-MM5, C-MM12, SMA1, and SMA2. The left-hand panel shows the 1.3 mm continuum image, corrected for the primary beam response, in grey-scale, overlaid with 3σ contours from the 1.3 mm continuum image prior to correction for the primary beam. These contours correspond to structures identified in the dendrogram analysis (Section 3.1). Structures are identified using a minimum threshold of 4σ ($1\sigma = 2$ mJy beam^{-1}) and a minimum number of 18 contiguous pixels, with a step increase of 1σ for further substructure to be identified. The black contours (left-hand panel) and corresponding black lines (tree diagram, right-hand panel) show an example of a parent tree structure with further substructure (in this case the structure containing C-MM5, SMA1, and SMA2). The green contour represents an additional branch within this structure, which hosts two cores, C-MM5 and SMA2. The red contours (left-hand panel) and corresponding red lines (tree diagram, right-hand panel) denote the highest level of a parent structure or of an independent structure with no further substructure if present. C-MM12 shows only parent structure and has no further substructure.

Table 1. Properties of millimetre continuum sources.

Source[a]	J2000.0 coordinates[b]		J2000.0 coordinates[c]		$R_{\rm eff}$[d]	$I_{\rm peak}$[e]	S_ν[f]
	$\alpha(^{\rm hms})$	$\delta(^\circ\,'\,'')$	$\alpha(^{\rm hms})$	$\delta(^\circ\,'\,'')$	(pc)	(mJy beam^{-1})	(mJy)
C-MM3	06 41 12.31	+09 29 11.50	06 41 12.28	+09 29 11.96	0.011	370	395
C-MM4	06 41 10.08	+09 29 21.70	06 41 09.95	+09 29 21.40	0.017	185	496
C-MM5	06 41 10.15	+09 29 33.70	06 41 10.14	+09 29 35.87	0.012	62	131
C-MM10	06 41 08.94	+09 29 44.56	06 41 08.75	+09 29 44.24	0.015	37	113
C-MM12	06 41 09.59	+09 29 54.64	06 41 09.63	+09 29 54.62	0.013	209	274
C-MM13	06 41 11.47	+09 29 17.47	06 41 11.51	+09 29 18.00	0.0099	34	53
SMA1	06 41 10.00	+09 29 49.25	06 41 10.12	+09 29 47.97	0.0079	15	21
SMA2	06 41 10.46	+09 29 39.66	06 41 10.46	+09 29 39.16	0.0057	27	26
SMA3	06 41 09.11	+09 29 26.50	06 41 09.16	+09 29 27.38	0.0093	17	31
SMA4	06 41 09.88	+09 29 14.53	06 41 09.88	+09 29 14.85	0.0053	48	36

Notes. [a]Sources identified in the dendrogram analysis: C-MM – denotes previously known/named millimetre sources (Peretto et al. 2006, 2007); SMA – denotes new 1.3 mm detections.
[b]Position of millimetre continuum peak.
[c]Position of intensity-weighted centroid, computed using *Computing Dendrogram Statistics* (Astropy Collaboration et al. 2013).
[d]Effective radius, computed from the total leaf area using *Computing Dendrogram Statistics* (Astropy Collaboration et al. 2013), through $R_{\rm eff} = \sqrt{\rm Area/\pi}$ and assuming the distance of 738pc to NGC 2264-C.
[e]Peak intensity of 1.3 mm continuum emission, corrected for the primary beam response.
[f]Integrated 1.3 mm flux density, measured from the primary-beam-corrected continuum image using CASAVIEWER and the 3σ mask from the dendrogram computed from the uncorrected image (see Section 3.1). For sources which are nested within parent structures (e.g. C-MM5, SMA1, and SMA2), only the flux from within the highest level of that structure (e.g. the leaves) is extracted (see the red contours in Fig. 3).

within the field of view shown in Fig. 2, only C-MM11 – which lies outside the 20 per cent power level of the SMA primary beam – is not detected in our SMA image. Our non-detection of C-MM11 is also consistent with the relative intensities of the millimetre continuum sources reported by Peretto et al. (2006, 1.2 mm IRAM 30-m observations): C-MM11 is the weakest Peretto et al. source within our SMA field (Fig. 1).

Our four new detections SMA1, SMA2, SMA3, and SMA4 have the lowest integrated flux densities of the 10 millimetre continuum sources: the brightest new detections (SMA3 and SMA4) have integrated flux densities that are approximately half that of the weakest previously reported source (C-MM13) in our SMA image (Table 1). This is consistent with SMA1-SMA4 not having been reported based on previous observations. We note that SMA4 is visible as a 3σ contour in fig. 1 of Peretto et al. (2007, PdBI 3.2 mm observations), but was considered a marginal detection and not studied further.

Inspecting the continuum map by eye reveals an additional millimetre continuum peak not identified by the dendrogram analysis. We separate C-MM5 into two cores: one at the peak position for C-MM5 tabulated in Table 1, and a second ∼4.5 arcsec north (see Fig. 2). The intensity of this second peak surpasses the dendrogram threshold for substructure; however, the number of contiguous pixels is below the set limit, so the leaf is merged into C-MM5. If the number of contiguous pixels required is reduced to 77 per cent of the area of the synthesized beam, C-MM5 is separated into two

Table 2. Molecular line transitions detected towards millimetre continuum peaks in NGC 2264-C.

Species	Transition	Frequency[a] (GHz)	E_{upper}[a] (K)	Detected[b] CMM3	CMM4	CMM5	CMM10	CMM12	CMM13	CMM5b	SMA1	SMA2	SMA3	SMA4
							LSB							
CH_3OH	5(1, 4)−4(2, 2)	216.946	55.9	N	Y	N	N	N	N	N	N	N	N	N
SiO	(5−4)	217.105	31.3	Y	Y	N	N	Y	N	Y	N	N	N	N
DCN	(3−2)	217.239	20.9	N	Y	Y	Y	N	N	Y	N	Y	N	N
c-C_3H_2[c]	$6_{16}-5_{05}$	217.822	38.6	N	Y	N	N	Y	N	N	N	Y	N	N
c-C_3H_2[c]	$6_{06}-5_{15}$	217.822	38.6	N	Y	N	N	Y	N	N	N	Y	N	N
c-C_3H_2	$5_{14}-5_{23}$	217.940	35.4	N	Y	N	N	N	N	N	N	Y	N	N
H_2CO	3(0, 3)−2(0, 2)	218.222	21.0	Y	Y	N	Y	Y	N	Y	N	Y	Y	N
HC_3N	(24−23)	218.324	131.0	N	Y	Y	N	N	N	Y	N	N	N	N
CH_3OH	4(2, 2)−3(1, 2)	218.440	45.5	N	Y	N	N	N	N	N	N	N	Y	N
H_2CO	3(2, 2)−2(2, 1)	218.476	68.1	N	Y	N	N	N	N	N	N	N	Y	N
H_2CO	3(2, 1)−2(2, 0)	218.760	68.1	Y	Y	N	N	Y	N	Y	N	Y	Y	N
OCS	(18−17)	218.903	99.8	N	Y	N	N	Y	N	N	N	N	N	N
$C^{18}O$	(2−1)	219.560	15.8	N	Y	N	Y	N	N	Y	Y	Y	Y	N
SO	6(5)−5(4)	219.949	35.0	N	Y	Y	N	Y	N	Y	N	Y	Y	N
CH_3OH	8(0, 8)−7(1, 6) E	220.078	96.6	N	Y	N	N	N	N	N	N	N	N	N
CH_3CN	(12_4-11_4)	220.679	183.3	N	N	Y[d]	N	N	N	N	N	N	N	N
CH_3CN	(12_3-11_3)	220.709	133.3	N	Y[d]	Y[d]	N	N	N	N	N	N	N	N
CH_3CN	(12_2-11_2)	220.730	97.4	N	Y[d]	Y[d]	N	N	N	N	N	N	N	N
CH_3CN[e]	(12_1-11_1)	220.743	76.0	N	Y	Y	N	N	N	N	N	N	N	N
CH_3CN[e]	(12_0-11_0)	220.747	68.8	N	Y	Y	N	N	N	N	N	N	N	N
							USB							
CH_3OH	8(−1, 8)−7(0, 7) E	229.759	89.1	N	Y	N	N	N	N	N	N	N	Y	N
CH_3OH	3(−2, 2)−4(−1, 4) E	230.027	39.8	N	Y	N	N	N	N	N	N	N	N	N
OCS	(19−18)	231.061	110.8	N	Y	N	N	N	N	N	N	N	N	N
^{13}CS	(5−4)	231.221	33.29	N	Y	N	N	N	N	N	N	Y	N	N

Notes. [a]From Splatalogue (http://www.splatalogue.net/), Müller et al. (2005).
[b]Y: detected at $\geq 5\sigma$, N: undetected (no emission at $\geq 5\sigma$). All measurements were made from image cubes corrected for the primary beam response, and a detection was determined from the spectra extracted from those beam corrected image cubes. Thus, for sources far from the pointing centre such as C-MM3, the rms noise is higher.
[c]These components are blended in the spectra and cannot be separated.
[d]CH_3CN components where emission is $<5\sigma$ but $>3\sigma$.
[e]These CH_3CN components are blended in the spectra: 'Y' indicates emission $>5\sigma$ for the blended line. See Table 3 for line fits.

leaves by the dendrogram analysis. Inspection of the molecular line emission also indicates these two leaves may be separate objects (Section 3.2). We therefore suggest that the northern leaf (hereafter C-MM5b) and C-MM5 are distinct millimetre continuum peaks, which we are unable to unequivocally separate at the resolution of our SMA data.

3.2 Molecular line emission

We detect molecular line emission in 23 transitions of 13 species above 5σ with the SMA, including SiO, CO and its isotopologues (^{13}CO and $C^{18}O$), SO, OCS, H_2CO, CH_3OH, DCN, c-C_3H_2, ^{13}CS, HC_3N, and CH_3CN. All lines detected at $>5\sigma$ have E_{upper} between ∼16 and 131 K. Table 2 lists the species, transition, rest frequency, E_{upper}, and whether the line is detected at $>5\sigma$ towards the millimetre continuum peak of each of the 11 cores (including C-MM5b, see Section 3.1). Table 3 presents the parameters (peak line intensity, line centre velocity, linewidth, and integrated line intensity) obtained from single Gaussian fits to lines detected at $>5\sigma$, at each millimetre continuum peak. No fits are presented for ^{12}CO and ^{13}CO due to the complexity of the line profiles, which are strongly affected both by self-absorption and by artefacts from poorly imaged large-scale emission; ^{12}CO and ^{13}CO are similarly excluded from Table 2.

Fig. 4 presents integrated intensity maps for all detected transitions, including ^{12}CO and ^{13}CO. The velocity range over which emission is integrated is determined for each transition, to encompass all channels with emission above 3σ. As shown in Fig. 4, the morphology of the detected line emission is complex. For many transitions, the spatial morphology of the line emission differs markedly from that of the millimetre continuum. The emission in the integrated intensity maps falls into three main categories: (i) 'compact' molecular line emission that directly traces millimetre continuum peaks, which includes emission from CH_3CN, OCS (18−17) and OCS (19−18), HC_3N, and the CH_3OH 5(1, 4)−4(2, 2), CH_3OH 8(0, 8)−7(1, 6) E and CH_3OH 3(−2, 2)−4(−1, 4) E transitions; (ii) 'diffuse' molecular line emission that overlaps but may not be clearly associated with millimetre continuum emission (e.g. may differ in morphology), which includes emission from c-C_3H_2, DCN and $C^{18}O$; and (iii) spatially extended molecular line emission that is more likely associated with outflows, which includes emission from SiO, SO, H_2CO, and the CH_3OH 4(2, 2)−3(1, 2) and CH_3OH 8(−1, 8)−7(0, 7) E transitions. Emission from ^{13}CS appears to fall into both the 'compact' (i) and 'diffuse' (ii) categories. As shown in Fig. 4, the velocity-integrated ^{12}CO and ^{13}CO emission extends across much of the field, ^{12}CO and ^{13}CO are therefore not included in these categories; high-velocity ^{12}CO, however, traces outflows, as discussed in Section 3.2.2.

A distinct feature, which we have labelled the 'ridge', is also evident in Fig. 4. The ridge is associated with the strongest H_2CO emission in the field, as well as the strongest emission in several CH_3OH transitions. While the southern edge of the ridge overlaps

Table 3. Gaussian fits to molecular lines detected at millimetre continuum peaks.

Species	Transition	Frequency	E_{upper}	Fitted line parameters			
				Peak intensity[a]	V_{centre}[a]	Linewidth[a]	$\int S\,dv$[a]
		(GHz)	(K)	(Jy beam^{-1})	(km s^{-1})	(km s^{-1})	(Jy beam^{-1} km s^{-1})
				C-MM3			
H_2CO[b]	3(0, 3)−2(0, 2)	218.222	21.0	0.91 (0.11)	6.60 (0.22)	3.93 (0.54)	3.80 (0.49)
H_2CO[b]	3(0, 3)−2(0, 2)	218.222	21.0	0.44 (0.08)	−6.50 (0.33)	4.72 (0.98)	2.22 (0.40)
H_2CO	3(2, 1)−2(2, 0)	218.760	68.1	0.58 (0.11)	8.22 (0.25)	2.68 (0.62)	1.66 (0.36)
				C-MM4			
CH_3OH	5(1, 4)−4(2, 2)	216.946	55.9	0.25 (0.03)	8.88 (0.15)	3.70 (0.35)	0.98 (0.12)
SiO[c]	(5−4)	217.105	31.3	0.22 (0.03)	15.04 (0.41)	5.33 (0.97)	1.26 (0.30)
DCN	(3−2)	217.239	20.9	0.87 (0.04)	8.53 (0.08)	3.54 (0.19)	3.29 (0.23)
c-C_3H_2	6_{16}−5_{05}	217.822	38.6	0.55 (0.03)	7.77 (0.06)	2.54 (0.15)	1.50 (0.08)
c-C_3H_2	5_{14}−5_{23}	217.940	35.4	0.24 (0.03)	8.70 (0.19)	2.92 (0.46)	0.74 (0.11)
H_2CO	3(0, 3)−2(0, 2)	218.222	21.0	1.75 (0.03)	7.62 (0.03)	3.3 (0.07)	6.14 (0.11)
HC_3N	(24−23)	218.324	131.0	0.21 (0.03)	8.11 (0.20)	3.88 (0.49)	0.85 (0.14)
CH_3OH	4(2, 2)−3(1, 2)	218.440	45.5	0.51 (0.03)	8.72 (0.11)	3.39 (0.26)	1.83 (0.13)
H_2CO	3(2, 2)−2(2, 1)	218.476	68.1	0.55 (0.03)	7.82 (0.11)	3.85 (0.26)	2.24 (0.14)
H_2CO	3(2, 1)−2(2, 0)	218.760	68.1	0.80 (0.03)	8.11 (0.06)	3.57 (0.14)	3.06 (0.11)
OCS	(18−17)	218.903	99.8	0.21 (0.02)	8.84 (0.33)	6.29 (0.89)	1.43 (0.18)
$C^{18}O$	(2−1)	219.560	15.8	2.59 (0.05)	8.03 (0.18)	2.38 (0.04)	6.57 (0.11)
SO	6(5)−5(4)	219.949	35.0	1.32 (0.05)	8.16 (0.05)	3.04 (0.13)	4.28 (0.17)
CH_3CN	(12_3−11_3)	220.709	133.3	0.10 (0.01)	5.77 (0.51)	2.76 (1.08)	0.28 (0.11)
CH_3CN	(12_2−11_2)	220.730	97.4	0.14 (0.01)	5.32 (0.4)	2.46 (0.80)	0.37 (0.10)
CH_3CN[d]	(12_1−11_1)	220.743	76.0	0.21 (0.01)	7.69 (0.28)	1.61 (0.53)	0.37 (0.10)
CH_3CN[d]	(12_0−11_0)	220.747	68.8	0.16 (0.01)	7.34 (0.29)	2.34 (0.59)	0.40 (0.10)
CH_3OH	8(0, 8)−7(1, 6) E	220.078	96.6	0.21 (0.03)	7.96 (0.30)	4.70 (0.73)	1.07 (0.15)
CH_3OH	8(−1, 8)−7(0, 7) E	229.759	89.1	0.36 (0.03)	8.29 (0.15)	4.06 (0.37)	1.54 (0.13)
CH_3OH	3(−2, 2)−4(−1, 4) E	230.027	39.8	0.22 (0.03)	8.32 (0.28)	4.35 (0.68)	1.02 (0.15)
OCS	(19−18)	231.061	110.8	0.27 (0.03)	8.42 (0.23)	4.07 (0.55)	1.19 (0.15)
^{13}CS	(5−4)	231.221	33.29	0.26 (0.04)	7.61 (0.30)	4.28 (0.74)	1.16 (0.19)
				C-MM5			
DCN	(3−2)	217.239	20.9	0.13 (0.02)	9.54 (0.22)	2.09 (0.56)	0.28 (0.10)
HC_3N	(24−23)	218.324	131.0	0.25 (0.02)	9.51 (0.08)	2.65 (0.28)	0.70 (0.06)
SO[b]	6(5)−5(4)	219.949	35.0	0.55 (0.05)	7.22 (0.70)	6.13 (1.73)	3.57 (1.06)
SO[b]	6(5)−5(4)	219.949	35.0	0.33 (0.01)	13.2 (0.08)	3.89 (0.21)	1.35 (0.09)
CH_3CN	(12_4−11_4)	220.679	183.3	0.12 (0.03)	8.82 (0.30)	2.68 (0.69)	0.34 (0.11)
CH_3CN	(12_3−11_3)	220.709	133.3	0.10 (0.02)	5.59 (0.46)	2.83 (1.20)	0.30 (0.10)
CH_3CN	(12_2−11_2)	220.730	97.4	0.11 (0.02)	7.26 (0.48)	4.05 (0.98)	0.49 (0.11)
CH_3CN[d]	(12_1−11_1)	220.743	76.0	0.12 (0.02)	7.51 (0.64)	2.78 (1.26)	0.35 (0.18)
CH_3CN[d]	(12_0−11_0)	220.747	68.8	0.20 (0.02)	8.51 (0.27)	3.61 (0.50)	0.78 (0.12)
				C-MM10			
DCN	(3−2)	217.239	20.9	0.38 (0.05)	7.80 (0.15)	2.07 (0.33)	0.84 (0.17)
H_2CO	3(0, 3)−2(0, 2)	218.222	21.0	1.09 (0.11)	7.71 (0.09)	1.59 (0.19)	1.85 (0.30)
$C^{18}O$	(2−1)	219.560	15.8	0.25 (0.04)	7.83 (0.26)	3.56 (0.61)	0.96 (0.22)
				C-MM12			
SiO[c]	(5−4)	217.105	31.3	0.65 (0.05)	10.93 (0.16)	4.36 (0.47)	3.03 (0.28)
c-C_3H_2	6_{16}−5_{05}	217.822	38.6	0.31 (0.06)	9.34 (0.20)	1.86 (0.38)	0.61 (0.12)
H_2CO	3(0, 3)−2(0, 2)	218.222	21.0	0.57 (0.09)	11.18 (0.28)	3.55 (0.66)	2.17 (0.54)
H_2CO	3(2, 1)−2(2, 0)	218.760	68.1	0.20 (0.02)	10.86 (0.14)	2.97 (0.33)	0.64 (0.10)
OCS	(18−17)	218.903	99.8	0.22 (0.02)	8.49 (0.18)	3.96 (0.42)	0.94 (0.13)
SO[b]	6(5)−5(4)	219.949	35.0	0.47 (0.06)	10.85 (0.29)	4.51 (0.70)	2.25 (0.46)
SO[b]	6(5)−5(4)	219.949	35.0	0.25 (0.03)	28.90 (0.28)	5.85 (0.67)	1.62 (0.24)
				SMA1			
$C^{18}O$	(2−1)	219.560	15.8	0.67 (0.08)	9.92 (0.11)	2.19 (0.29)	1.59 (0.28)
				SMA2			
DCN	(3−2)	217.239	20.9	0.36 (0.04)	9.95 (0.18)	3.23 (0.42)	1.23 (0.21)
c-C_3H_2[e]	6_{16}−5_{05}	217.822	38.6	0.27 (0.03)	9.42 (0.13)	2.78 (0.31)	0.81 (0.12)
c-C_3H_2	5_{14}−5_{23}	217.940	35.4	0.25 (0.03)	10.38 (0.15)	2.54 (0.34)	0.67 (0.12)
H_2CO	3(0, 3)−2(0, 2)	218.222	21.0	0.56 (0.04)	9.72 (0.10)	3.31 (0.25)	2.00 (0.20)
H_2CO	3(2, 1)−2(2, 0)	218.760	68.1	0.19 (0.03)	9.88 (0.23)	2.89 (0.53)	0.58 (0.14)
$C^{18}O$	(2−1)	219.560	15.8	1.73 (0.06)	9.68 (0.05)	2.70 (0.11)	4.97 (0.27)
SO	6(5)−5(4)	219.949	35.0	0.80 (0.02)	9.52 (0.02)	2.16 (0.06)	1.82 (0.06)
^{13}CS	(5−4)	231.221	33.29	0.39 (0.05)	9.52 (0.12)	2.06 (0.28)	0.85 (0.15)

Table 3 – *continued*

Species	Transition	Frequency (GHz)	E_{upper} (K)	Fitted line parameters: Intensity[a] (Jy beam^{-1})	V_{centre}[a] (km s^{-1})	Width[a] (km s^{-1})	$\int S\,dv$[a] (Jy beam^{-1} km s^{-1})
			SMA3				
H_2CO	3(0, 3)−2(0, 2)	218.222	21.0	2.48 (0.08)	8.96 (0.08)	4.59 (0.18)	12.08 (0.63)
CH_3OH	4(2, 2)−3(1, 2)	218.440	45.5	1.08 (0.07)	8.55 (0.08)	2.56 (0.20)	2.94 (0.30)
H_2CO	3(2, 2)−2(2, 1)	218.476	68.1	1.30 (0.04)	8.83 (0.05)	3.47 (0.12)	4.80 (0.21)
H_2CO	3(2, 1)−2(2, 0)	218.760	68.1	1.20 (0.04)	8.81 (0.05)	3.56 (0.12)	4.58 (0.12)
$C^{18}O$	(2−1)	219.560	15.8	0.39 (0.04)	8.83 (0.23)	4.84 (0.54)	2.01 (0.30)
SO[e]	6(5)−5(4)	219.949	35.0	0.43 (0.06)	9.93 (0.41)	6.26 (0.96)	2.84 (0.57)
CH_3OH	8(−1, 8)−7(0, 7) E	229.759	89.1	0.97 (0.04)	8.60 (0.07)	3.40 (0.17)	3.52 (0.23)
			C-MM5b				
SiO	(5−4)	217.105	31.3	0.34 (0.03)	14.61 (0.16)	4.15 (0.37)	1.49 (0.17)
DCN	(3−2)	217.239	20.9	0.94 (0.05)	9.31 (0.07)	2.52 (0.17)	2.51 (0.22)
H_2CO	3(0, 3)−2(0, 2)	218.222	21.0	0.68 (0.06)	8.93 (0.09)	2.22 (0.22)	1.60 (0.21)
HC_3N	(24−23)	218.324	131.0	0.44 (0.03)	8.97 (0.07)	2.11 (0.17)	0.99 (0.11)
H_2CO	3(2, 1)−2(2, 0)	218.760	68.1	0.12 (0.02)	9.63 (0.22)	4.11 (0.52)	0.54 (0.09)
$C^{18}O$	(2−1)	219.560	15.8	1.54 (0.08)	9.28 (0.06)	2.39 (0.13)	3.92 (0.29)
SO[b]	6(5)−5(4)	219.949	35.0	0.39 (0.07)	9.83 (0.17)	2.18 (0.47)	0.90 (0.24)
SO[b]	6(5)−5(4)	219.949	35.0	0.14 (0.03)	15.32 (0.21)	3.12 (0.51)	0.48 (0.10)

Notes. [a]Formal errors from the single Gaussian fits are given in the brackets.
[b]Two distinct velocity components are present in the spectrum; a single Gaussian fit is reported for each component.
[c]Two velocity components appear to be present in the spectrum, but are not sufficiently well separated in velocity to be fit separately. The reported fit is for the stronger component.
[d]The $k = 0$ and 1 CH_3CN components are blended in the spectra. The reported parameters are from multiple-Gaussian fits using the GILDAS CLASS package.
[e]Complex line profile, not well fit by a single Gaussian.

SMA3, the majority of the ridge structure does not appear to be associated with a millimetre continuum source. The nature of this intriguing feature is discussed in Section 4.2.

3.2.1 Line emission associated with millimetre continuum sources: systemic velocity estimates

As shown in Fig. 4, compact molecular line emission that peaks at the millimetre continuum peaks is seen in only a few lines (OCS, CH_3CN, HC_3N, and the 216.946 GHz, 220.078, and 230.027 GHz CH_3OH transitions), and only towards C-MM4, C-MM5, and C-MM5b (not all of these lines are detected towards all three sources; see Table 2). For these sources, we present estimates of the v_{LSR}'s of the individual millimetre continuum cores in Table 4, based on the fits (Table 3) to lines that exhibit spatially compact emission. We note that for CH_3CN, the ladder transitions with a detection $<5\sigma$ are excluded from the v_{LSR} estimates.

DCN and c-C_3H_2 exhibit more extended emission (which we refer to as 'diffuse') that is coincident with, and morphologically similar to, the millimetre continuum emission of C-MM4 and SMA2. For C-MM4, in particular, the similar morphologies of the line and millimetre continuum emission suggest that this more extended molecular line emission is associated with the millimetre continuum source. Strong DCN emission is also detected in the vicinity of C-MM5 and C-MM5b, but in this case the morphology of the line emission differs from that of the millimetre continuum, so it is not clear that the DCN emission is directly associated with the continuum source(s). Table 4 presents estimates of core v_{LSR}'s based on fits to lines that exhibit 'diffuse' emission (including $C^{18}O$ as well as DCN and c-C_3H_2) and are detected at the position of a given core's millimetre continuum peak. We emphasize that while this approach allows us to estimate v_{LSR}'s for more sources, the results must be treated with greater caution than the estimates based on compact molecular line emission. The morphology of the $C^{18}O$ emission, for example, does not match that of the millimetre continuum, suggesting that the detected $C^{18}O$ may not arise from the dense gas of the millimetre continuum cores. Our v_{LSR} estimates exclude lines that likely trace outflows and exhibit clearly extended emission (e.g. SiO, SO, H_2CO, and the remaining CH_3OH lines).

The v_{LSR}'s of the millimetre continuum sources, estimated as described above, range from ∼7.8 to 9.9 km s^{-1}. For C-MM4 and C-MM5 (for which we have the most data from line fits, see Tables 3 and 4), the v_{LSR} estimates based on compact and 'diffuse' tracers differ by up to ∼1 km s^{-1} (for C-MM5), and the standard deviation of the v_{LSR}'s measured from individual lines is ∼0.5 km s^{-1} (Table 4).

Towards C-MM3, C-MM13, SMA1, and SMA4 no emission is detected from lines that exhibit either 'compact' or 'diffuse' morphology. As a result, we cannot estimate the v_{LSR}'s of these sources from our SMA data. v_{LSR} estimates for C-MM3 and C-MM13 are of particular interest, given the outflow activity near C-MM3 (Section 3.2.2) and the velocity gradient reported by Peretto et al. (2007) in NGC 2264-C (spanning C-MM2, C-MM3, C-MM13, and C-MM4). Since we are unable to estimate v_{LSR}'s for several continuum sources from our SMA data (and have robust estimates based on compact molecular line emission for only a small minority), we adopt the following approach. For C-MM4, where we have the most detected compact emission, we use our estimate of the v_{LSR} of 8.3 km s^{-1} for the remaining analysis. For C-MM3 and C-MM13, we adopt the v_{LSR}'s reported by Peretto et al. (2007) based on $N_2H^+(1-0)$ emission (Table 4). For the remaining millimetre continuum sources, we adopt the average v_{LSR} from our SMA data (averaged across all cores, for both compact and diffuse tracers) of 8.9 km s^{-1}. We note that for C-MM10 and C-MM5b, we have

multiple, consistent velocity measurements from our SMA data (though for C-MM10 only from 'diffuse' tracers); however, as these cores show no evidence of outflow activity, we adopt the three $v_{\rm LSR}$'s described above for simplicity in plotting composite maps of red and blueshifted emission (e.g. Fig. 6). The $v_{\rm LSR}$ adopted for each continuum peak, and used throughout the remainder of this paper, is given in Table 4.

3.2.2 Extended and high velocity molecular line emission: molecular outflows

As shown in Fig. 4, several species are characterized by collimated, extended emission: SiO, SO, CH_3OH, H_2CO, and ^{12}CO. The two most prominent collimated emission features in the integrated intensity maps (both elongated N-S) appear to be centred on C-MM3

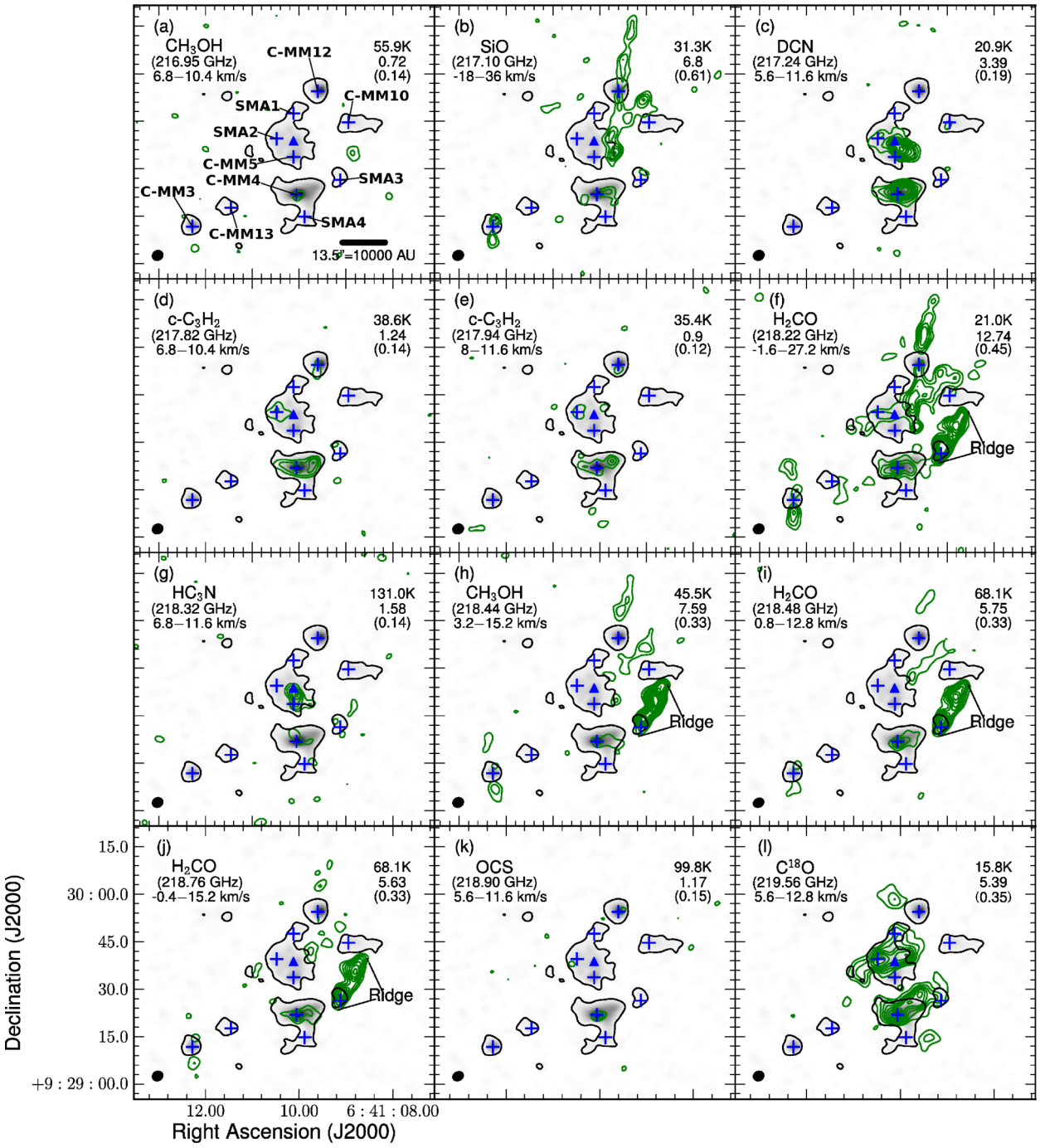

Figure 4. SMA integrated intensity maps (green contours) of detected molecular lines, overlaid on the 1.3 mm continuum emission (grey-scale and black contour, contour level $3\sigma = 6$ mJy beam^{-1}). The integrated velocity range is given in the top-left corner of each panel, along with the molecule and line rest frequency. $E_{\rm upper}$ for the transition and the peak and rms of each map (both in Jy beam^{-1} km s^{-1}) are given at upper right in each panel. Blue pluses (+) mark the positions of the millimetre continuum peaks from Table 1, and the blue triangle marks the position of C-MM5b (see Section 3.1). Contour levels for the integrated intensity maps are from 3σ to peak in steps of 2σ. Panel (p) shows the CH_3CN emission integrated over the $k = 0$–4 components and thus the velocity range and frequency is not given.

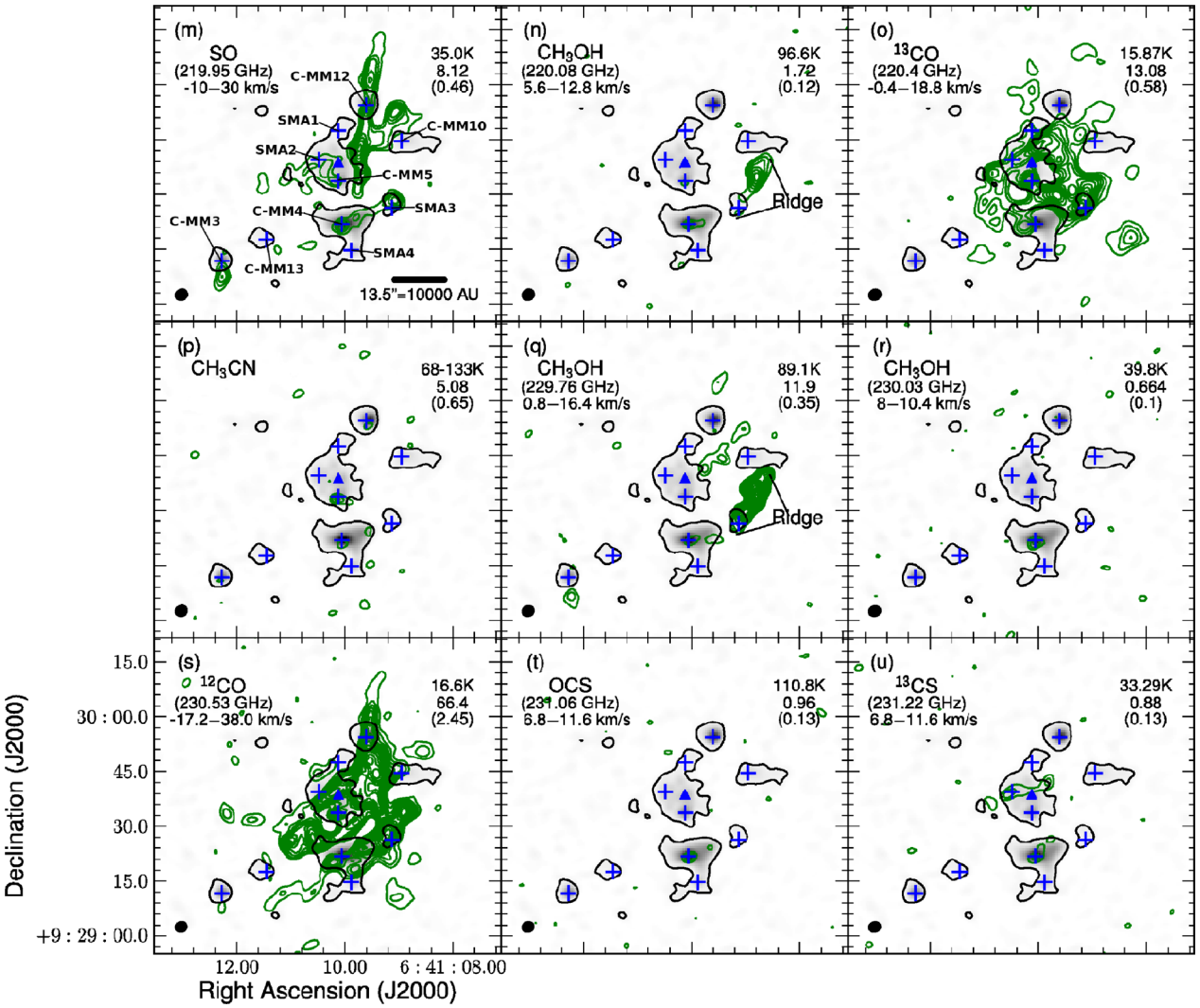

Figure 4 – *continued*

and C-MM12. To investigate the nature of the extended molecular line emission, and its relation to outflows previously reported based on lower angular resolution data, we analyse its velocity structure. To identify potential outflow axes, we use our high-resolution SMA observations of the well-known outflow tracer SiO (e.g. Gusdorf et al. 2008a,b; Guillet et al. 2009; Leurini et al. 2014, and references therein).

Fig. 5 presents integrated intensity maps of the red- and blueshifted SiO emission observed with the SMA (SiO (5−4), resolution ∼3 arcsec) and the JCMT (SiO (8−7), resolution ∼15 arcsec). We compare the SMA and JCMT data to test whether the spatial filtering of the SMA misses any large-scale active outflows (which would be seen in SiO emission with the JCMT). The JCMT observations (Fig. 5a) reveal two potential outflow systems: one encompassing both C-MM3 and C-MM13 (with the peak emission nearest to C-MM3), and a second that intersects both C-MM10 and C-MM12. In the second system, only blueshifted emission is detected with the JCMT; however, receiver H14 was not operational during our observations, resulting in a gap in the JCMT map north of C-MM12. Fig. 5(b) presents the higher spatial resolution SMA SiO (5−4) data. With the SMA, the SiO emission near C-MM3 and C-MM13 is clearly resolved, revealing a single bipolar outflow centred on C-MM3 (outflow axis A1, Fig. 5b). The red and blueshifted lobes are spatially well separated and are centred on the continuum source, indicating that the high-velocity SiO (5−4) emission traces a bipolar molecular outflow. The second potential outflow system identified in the JCMT data, towards C-MM12 and C-MM10, splits into multiple components at the higher spatial resolution of the SMA observations. As shown in Fig. 5(b), the SMA data reveal a collimated, bipolar outflow centred on C-MM12 (axis A2, Fig. 5b): as in the C-MM3 outflow, the red and blueshifted lobes are spatially well separated and centred on the millimetre continuum source. For both outflows, the sense of the velocity gradient is consistent in the SMA and JCMT observations (e.g. the blueshifted lobe is north of C-MM3, and the redshifted lobe south of C-MM3, in both the SMA and JCMT maps). The fact that our SMA SiO data recover (and resolve) both of the SiO outflows identified with the JCMT is strong evidence that the SMA is not 'missing' large-scale active outflows.

In addition to the two clear outflows driven by C-MM3 and C-MM12 along axes A1 and A2, there are several additional components of SiO emission present in the field, labelled 9–14 in Fig. 5. To the north of C-MM10, red- and blueshifted emission are present (components 9 and 10). Redshifted emission also extends through

Table 4. Systemic velocity estimates for 1.3 mm continuum sources.

Source	v_{LSR} (km s^{-1})			
	Compact[a]	Diffuse[b]	N_2H^+[c]	Adopted[d]
C-MM3	–	–	7.1	7.1
C-MM4	8.2 (0.5)	8.3 (0.4)	8.9	8.3
C-MM5	8.5 (1.0)	9.5	–	8.9
C-MM10	–	7.8 (0.02)	–	8.9
C-MM12	8.5	9.3	–	8.9
C-MM13	–	–	8.2	8.2
SMA1	–	9.9	–	8.9
SMA2	–	9.8 (0.4)	–	8.9
SMA3	–	8.8	–	8.9
SMA4	–	–	–	8.9
C-MM5b	9.0	9.3 (0.02)	–	8.9

Notes. [a]Average v_{LSR} estimates from molecular lines categorized as exhibiting 'compact' emission (see Section 3.2) and includes emission from CH_3CN (note only CH_3CN transitions with $>5\sigma$ detections are included), OCS, HC_3N, and CH_3OH 5(1, 4)−4(2, 2), CH_3OH 8(0, 8)−7(1, 6) E, and CH_3OH 3(−2, 2)−4(−1, 4) E. Note that not all of these lines are detected at $>5\sigma$ towards each core; see Table 2. Furthermore, ^{13}CS is not used in the v_{LSR} estimate for 'compact' emission as it also displays diffuse emission. The standard deviation is given in the brackets. If no value is given, emission was detected only in one transition.

[b]Average v_{LSR} estimates from molecular lines categorized as exhibiting 'diffuse' emission (see Section 3.2) and includes emission from $C^{18}O$, DCN, and c-C_3H_2. Again ^{13}CS is not used in the v_{LSR} estimate for 'diffuse' tracers as it also appears to trace compact emission. Note that not all of these lines are detected towards each core; see Table 2. The standard deviation is given in the brackets. If no value is given, emission was detected only in one transition.

[c]Taken from Peretto et al. (2007).

[d]v_{LSR} adopted for each core for the remainder of the analysis.

the blueshifted axis of A2 to C-MM5b (component 11). In addition, extended redshifted SiO emission is observed towards C-MM4 (components 13 and 14) and redshifted emission is found coincident with SMA3 (component 12). The nature of this additional SiO emission is unclear.

To further explore the nature and structure of the high-velocity outflow emission in NGC 2264-C, we consider four velocity regimes (e.g. Santiago-García et al. 2009): systemic (v_{LSR} ± 3 km s^{-1}), standard high velocity (SHV, v_{LSR} ± 3 to 10 km s^{-1}), intermediate high velocity (IHV, v_{LSR} ± 10–30 km s^{-1}), and extremely high velocity (EHV, v_{LSR} ± 30–50 km s^{-1}). Fig. 6 presents SMA integrated intensity maps for the systemic, SHV, and IHV regimes for SiO (5−4), SO (6(5)−5(4)), H_2CO (3(0, 3)−2(0, 2)), and ^{12}CO (2−1). These are the only four transitions in which emission is detected at velocities >10 km s^{-1} from the v_{LSR} (e.g. in the IHV regime). We do not present EHV maps because very little EHV emission is detected: the only $>3\sigma$ emission with $|v - v_{LSR}| > 30$ km s^{-1} is ^{12}CO (2−1) at ∼31 km s^{-1}, towards the redshifted lobe of the C-MM3 outflow. As described in Section 3.2.1, above, we adopt a v_{LSR} of 7.1 km s^{-1} for C-MM3 and a v_{LSR} of 8.3 km s^{-1} for the region covering C-MM4 (including C-MM13). For the rest of the region, the velocity ranges are calculated with respect to a $v_{LSR} = 8.9$ km s^{-1} (adopted for the other continuum cores, Section 3.2.1).

Towards the outflow axis A2, low-velocity (systemic) emission is traced by SiO, SO, and H_2CO (as shown in Fig. 6). In contrast, along axis A1 only H_2CO is detected at low velocities. In addition, two CH_3OH lines (CH_3OH 4(2,2)−3(1,2) and CH_3OH 8(−1,8)−7(0,7)E) exhibit extended emission along the outflow axes (see Fig. 4) only in the systemic and SHV regimes, and so are not shown in Fig. 6. There is also a noticeable extension in the systemic emission from SO and H_2CO running from north-west to south-east coincident with the components 9–11.

In the SHV regime, collimated red- and blueshifted emission centred on C-MM3 and C-MM12 is detected in SiO, SO, and H_2CO. The IHV ^{12}CO emission displays a similar morphology, consistent with the SHV and IHV molecular line emission tracing bipolar molecular outflows driven by these two millimetre continuum cores. (The ^{12}CO emission in the SHV regime is affected by poorly imaged extended structure and confusion with the surrounding cloud, making it difficult to identify outflows in ^{12}CO in this velocity range.) Both lobes of the outflow associated with C-MM3 are also detected in the IHV regime in SiO and SO, while only the redshifted lobe of the outflow associated with C-MM12 is detected in IHV SiO, SO, and H_2CO emission (Fig. 6).

The additional SiO components (numbered 9–14 in Fig. 5) are also associated with SHV SO and H_2CO emission, with the exception of the redshifted emission towards C-MM4. Redshifted SHV SiO emission is observed towards both C-MM4 and SMA3 (components 12–14), while (redshifted) SO and H_2CO emission are only observed towards SMA3 (component 12). In the IHV regime, only ^{12}CO emission is detected towards these components. While both redshifted (near SMA3) and blueshifted (south of C-MM4) emission are present, these potential lobes are not centred on a millimetre continuum source and it is unclear if they are related to a single outflow. Compared to the two bipolar outflows (along A1 and A2), the velocity extent of the emission towards the additional, ambiguous SiO components is also more modest. For ^{12}CO (2−1), the maximum redshifted velocity is ∼38, 32, 28, and 24 km s^{-1} for A1 (C-MM3 outflow, components 1–3), A2 (C-MM12 outflow, components 4–8), towards C-MM10/C-MM5b (components 9–11) and towards C-MM4/SMA3 (components 12–14), respectively. The minimum velocity for blueshifted ^{12}CO emission is −17.2 km s^{-1} for A1 (C-MM3 outflow) and −2.8 km s^{-1} for A2 (C-MM12 outflow) and towards C-MM4.

To examine the outflow kinematics in greater detail, Fig. 7 presents SiO, SO, H_2CO, and ^{12}CO spectra at the positions labelled in Fig. 5, along the potential outflow axes A1 and A2 (numbered 1–8), and towards the additional components (numbered 9–14). Works by Codella et al. (2014), Tafalla et al. (2010), and Lee et al. (2010) identified similarities between SiO and SO emission at high velocities. As shown in Fig. 6, SiO and SO exhibit similar morphologies in NGC 2264-C; however, the SiO emission extends to higher absolute velocities compared with the SO emission (e.g. for SiO the maximum red- and blueshifted velocities are 37 and −20 km s^{-1}, respectively, compared with 32 and −13 km s^{-1} for SO). Close examination of the line profiles also reveals a velocity gradient in ^{12}CO towards C-MM4 and SMA3, from redshifted (component 12) to blueshifted (component 14). This ^{12}CO emission is lower velocity than observed towards axes A1 and A2. The SiO emission is also considerably narrower towards C-MM4 and SMA3 than along axes A1 and A2.

We note that SiO (5−4) emission associated with outflows from low-mass (proto)stars is unlikely to be detected as extended, collimated structure in our SMA observations. Scaling the results of Gómez-Ruiz et al. (2013) and Codella et al. (2014) to the distance of NGC 2264-C and our SMA beam, we would detect only the strongest SiO (5−4) emission, and that at the ∼4σ–8σ level. We also note that in both the JCMT and SMA observations, the width of the collimated emission appears to be limited by the size of the beam.

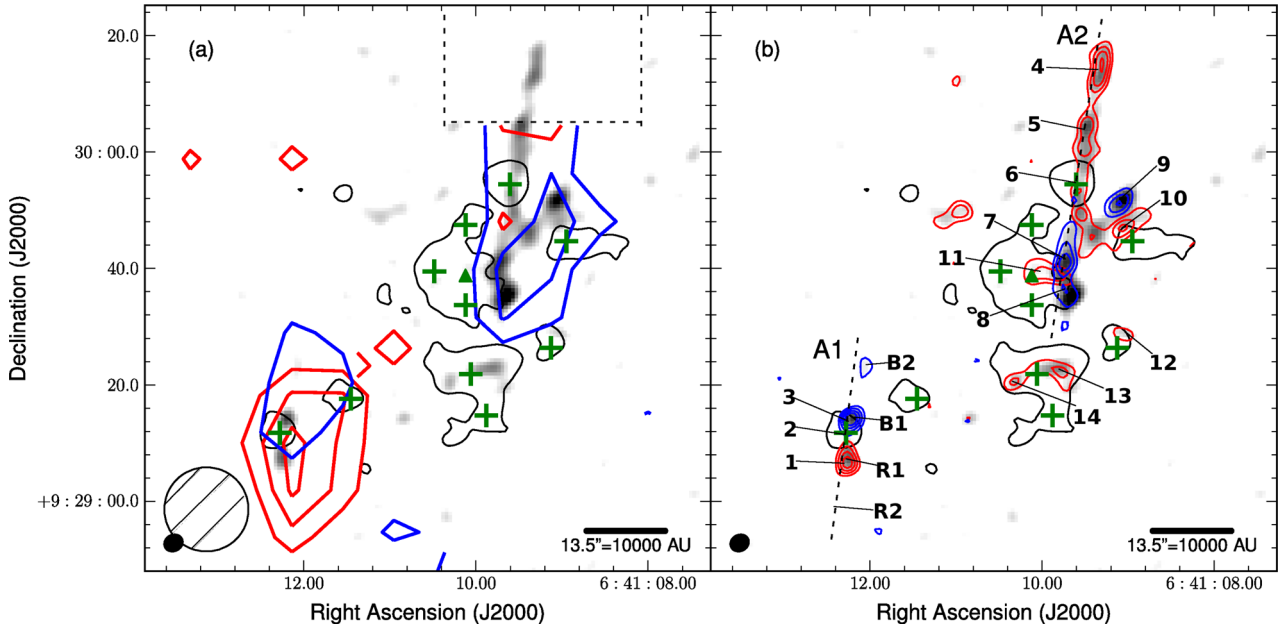

Figure 5. SiO kinematics. SMA SiO integrated intensity map (grey-scale, integrated over the velocity range −20 to 37 km s^{-1}) overlaid with contours of 1.3 mm continuum emission (black contour, level $3\sigma = 6$ mJy beam^{-1}) and blue/redshifted SiO emission from (a) the JCMT (SiO (8−7)) and (b) the SMA (SiO (5−4)). The velocity intervals for the blue/redshifted SiO begin 3 km s^{-1} from the $v_{\rm LSR}$ ($v_{\rm LSR}$ = 7.1 km s^{-1} for C-MM3, 8.3 km s^{-1} for C-MM4 and 8.9 km s^{-1} for C-MM12, see Section 3.2.1) and extend to the maximum outflow velocity. The velocity intervals are the same for the JCMT and SMA data and are: blue: −20 to +4.1 km s^{-1} for C-MM3 (and C-MM13), −1.0 to +5.3 km s^{-1} for C-MM4, and −20 to +5.9 km s^{-1} for C-MM12 (and the other millimetre continuum cores); red: +10.1 to +37 km s^{-1} (C-MM3 and C-MM13), +11.3 to +20 km s^{-1} (C-MM4), and +11.9 to +32 km s^{-1} (C-MM12 and other cores). In both panels, green pluses (+) mark the positions of the 10 millimetre continuum peaks from the dendrogram analysis and the green triangle marks the position of C-MM5b. (a) JCMT SiO (8−7) contour levels: (3,5,7,9) × σ = 0.2 K km s^{-1}. The 14.5 arcsec JCMT beam (hatched circle) and the SMA synthesized beam (filled ellipse) are shown at lower left. The dashed rectangle shows the area of missing data from the HARP receiver element H14. (b) SMA SiO (5−4) contour levels: (3,5,7,9) × σ = 0.36 Jy beam^{-1} km s^{-1}. The dashed black lines represent the possible outflow axes A1 and A2. The numbered positions 1–14 mark the components discussed in Section 3.2.2, and mark the positions at which the spectra shown in Fig. 7 were extracted. Positions 1–3 are part of the outflow axis A1, positions 4–8 are part of outflow axis A2, and the remaining positions mark locations of ambiguous SiO emission that is not obviously associated with an outflow. The labels R1, R2, B1, and B2 mark the components of the redshifted and blueshifted outflow lobes of C-MM3 named by Saruwatari et al. (2011).

3.2.3 Candidate millimetre CH_3OH masers

A notable feature of Fig. 4 is the very strong 229.759 GHz CH_3OH emission associated with the 'ridge'. The 229.759 GHz CH_3OH 8(−1, 8)−7(0, 7)E transition is a known class I methanol maser, first reported towards DR21 (OH) and DR21 west by Slysh, Kalenskiĭ & Val'tts (2002) based on observations with the IRAM 30-m telescope. Probable maser emission in this transition is often seen in SMA observations of massive star-forming regions (e.g. Fontani et al. 2009; Qiu & Zhang 2009; Cyganowski et al. 2011, 2012; Fish et al. 2011, and references therein). Most recently, Hunter et al. (2014) directly demonstrated the maser nature of 229.759 GHz CH_3OH emission in NGC6334I(N), by showing that the observed line brightness temperature ($T_{\rm B}$) is greater than the upper energy of the transition ($E_{\rm upper}$) in very high-resolution SMA observations.

To investigate the nature of the 229.759 GHz CH_3OH emission in NGC 2264-C, Fig. 8 presents integrated intensity maps and corresponding line profiles for the CH_3OH 8(−1, 8)−7(0, 7) E, CH_3OH 8(0, 8)−7(1, 6) E and CH_3OH 3(−2, 2)−4(−1, 4) E transitions at three locations where the CH_3OH 8(−1, 8)−7(0, 7) E 229.759 GHz emission is strongest. These are the ridge, the redshifted outflow lobe of C-MM3, and the redshifted outflow lobe of C-MM12. As shown in Fig. 8, the 229.759 GHz CH_3OH emission in the ridge is more than twice as strong as that towards the redshifted outflow lobe of either C-MM3 or C-MM12.

Like most previous 229 GHz studies (with the notable exception of Hunter et al. 2014), our SMA observations do not have sufficient angular resolution to establish masing in the 229.759 GHz line based on its brightness temperature. Slysh et al. (2002) proposed the ratio of the 229.759 GHz and 230.027 GHz CH_3OH lines as a diagnostic of maser emission, with values of 229.759/230.027 > 3 indicating non-thermal 229.759 GHz emission. We note that the 230.027 GHz line is undetected at all three positions, and the 3σ limits are used to calculate the line ratios (see Table 5 for the 3σ limits towards each position). At two positions in our field, this line ratio is ≥3: towards the redshifted lobe of the C-MM3 outflow, where the ratio is ∼3, and towards the strongest 229.759 GHz emission in the ridge, where the ratio is considerably higher (∼47). Furthermore, throughout the ridge the line ratio is consistently >8. While the line ratios towards the ridge are considerably higher than towards the C-MM3 outflow, the ridge line ratios fall within the range of line ratios, ∼7–100, found towards the outflow lobes of two extended green objects by Cyganowski et al. (2011). By comparison, the line ratio towards the C-MM4 continuum peak is <2, consistent with thermal emission from warm gas (Section 4.1.1).

Table 5 presents fits to the 220.078, 229.759, and 230.027 GHz CH_3OH lines at the three positions shown in Fig. 8. Emission from 229 GHz CH_3OH masers often coincides spatially and spectrally with emission in lower frequency class I CH_3OH maser transitions (e.g. Fish et al. 2011; Cyganowski et al. 2011, 2012). Class I CH_3OH maser emission, in the form of the 44 GHz transition,

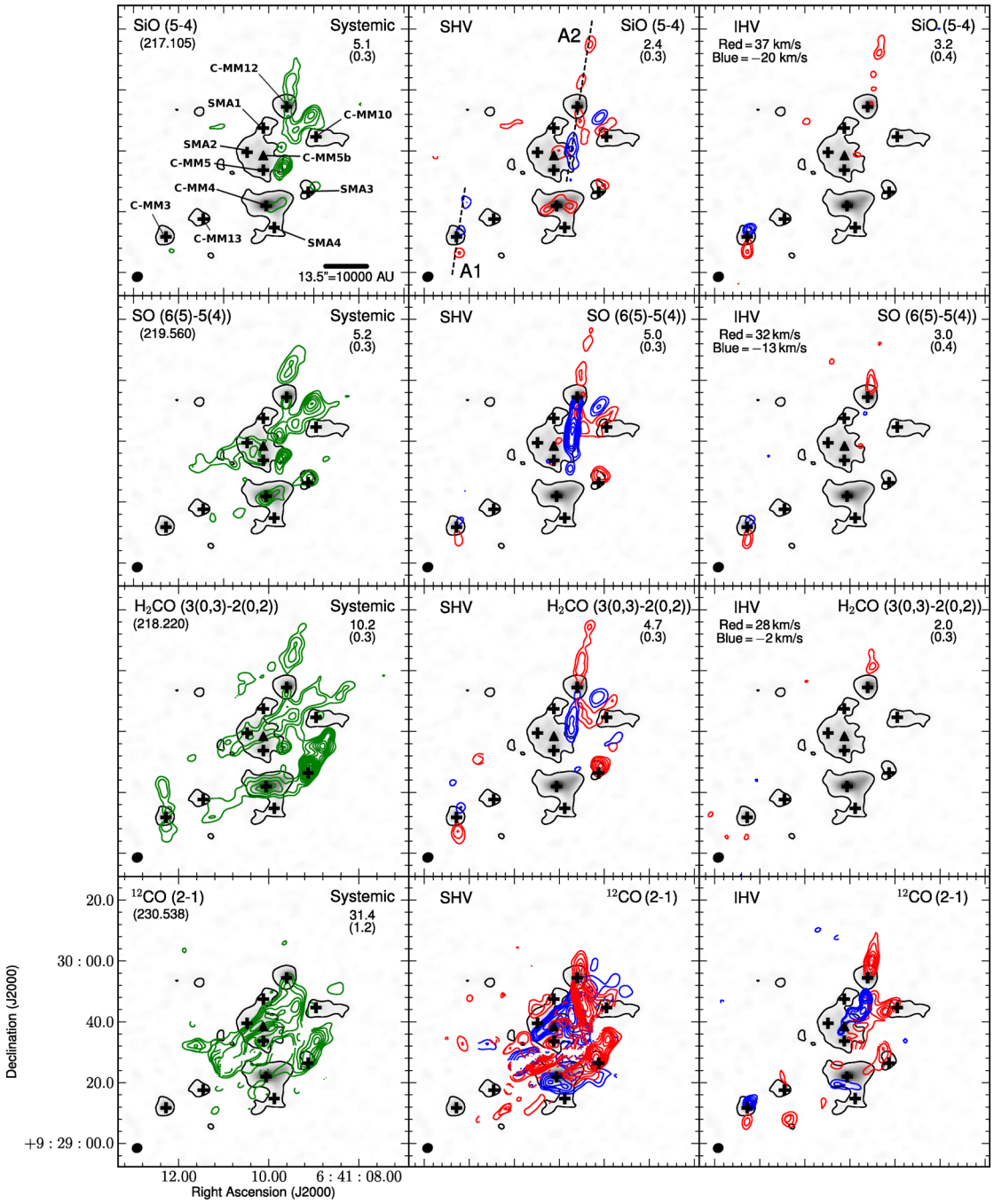

Figure 6. Integrated intensity maps (coloured contours) of emission at systemic (left-hand column), SHV (middle column) and IHV (right-hand column) velocities for the indicated transitions, overlaid on the SMA 1.3 mm continuum image (grey-scale and black contour, contour level $3\sigma = 6$ mJy beam^{-1}). 'Systemic' is defined as $v_{\rm LSR} \pm 3$ km s^{-1} (green contours), SHV as $v_{\rm LSR} \pm 3$–10 km s^{-1}, and IHV as $v_{\rm LSR} \pm >10$ km s^{-1} (where red and blue contours represent the red and blueshifted emission, respectively). The maps shown are composites, with an adopted $v_{\rm LSR}$ of 7.1 km s^{-1} for C-MM3, 8.3 km s^{-1} for C-MM4 (including the vicinity of C-MM13), and 8.9 km s^{-1} for the remainder of the map (Section 3.2.1). The maximum velocity extent of the emission is given at top left in the IHV panels, except for ^{12}CO (2−1), where the maximum velocity differs significantly from outflow to outflow across the map (see Section 3.2.2). Contour levels are shown as 3σ, 5σ, and then to peak, increasing in steps of 3σ. The peak and rms (in Jy beam^{-1} km s^{-1}) are given at upper right in each panel, except for SHV and IHV ^{12}CO. For ^{12}CO (2-1), the contoured rms levels are: SHV, red: 1.9 Jy beam^{-1} km s^{-1} (C-MM3/C-MM13), 1.9 Jy beam^{-1} km s^{-1} (other sources); SHV, blue: 1.4 Jy beam^{-1} km s^{-1} (C-MM3/C-MM13), 1.9 Jy beam^{-1} km s^{-1} (other sources); IHV, red: 1.0 Jy beam^{-1} km s^{-1} (C-MM3/C-MM13), 1.4 Jy beam^{-1} km s^{-1} (other sources); IHV, blue: 0.4 Jy beam^{-1} km s^{-1} (C-MM3/C-MM13), 0.6 Jy beam^{-1} km s^{-1} (other sources). In all panels, black pluses (+) mark the positions of the 10 millimetre continuum peaks from the dendrogram analysis, and the black triangle marks the position of C-MM5b. The outflow axes from Fig. 5(b) are overlaid for reference in the top middle panel (SHV SiO). The ^{12}CO emission in the systemic and SHV panels shows a discontinuity in the emission to the north of C-MM4, this is due to the composite of the different velocity ranges used when integrating the emission towards the continuum peaks and given the CO emission is more abundant over the field than the other molecular transitions.

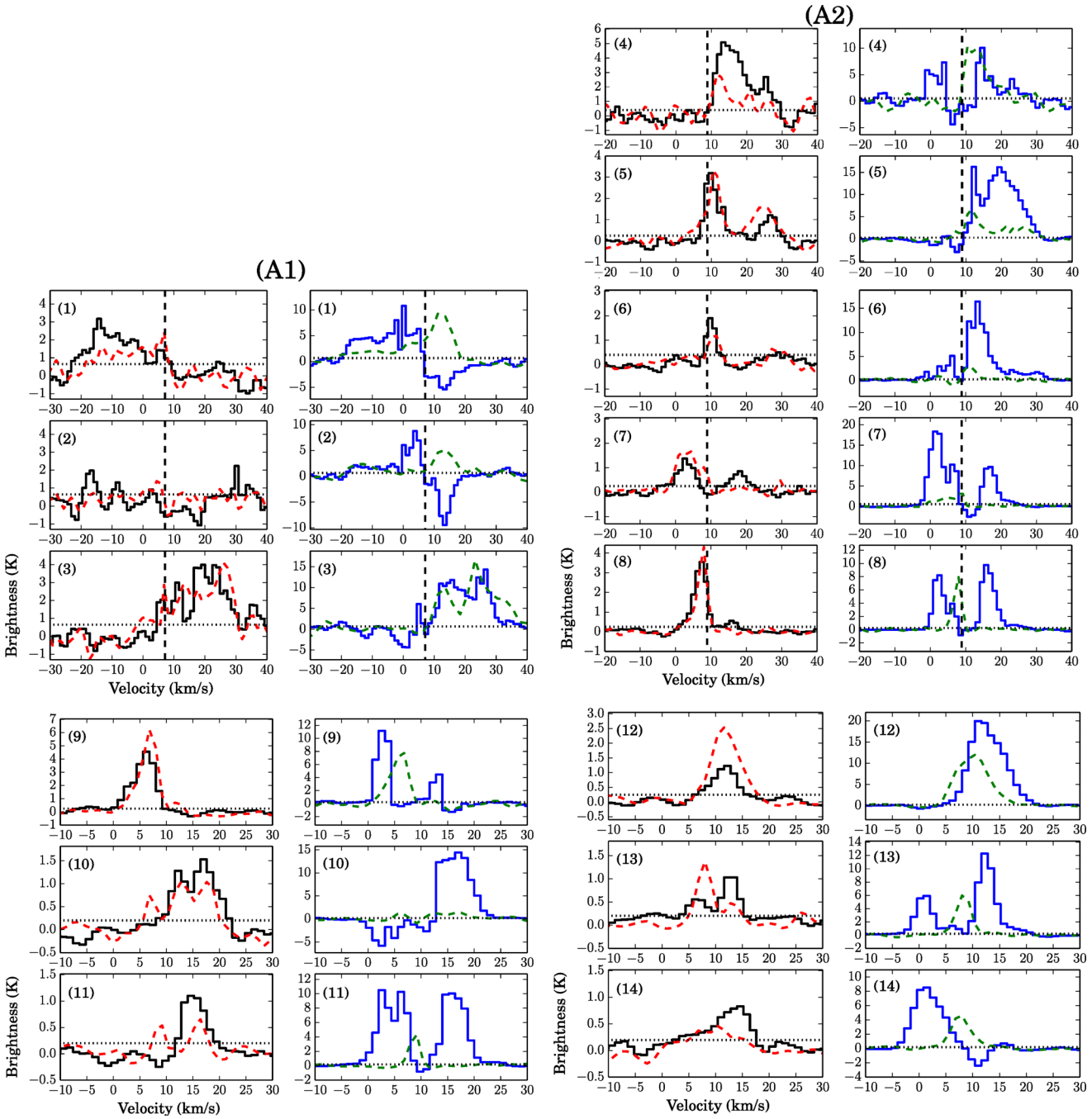

Figure 7. Spectra of SiO (5−4), SO 6(5)−5(4), H_2CO 3(0, 3)−2(0, 2) and ^{12}CO (2−1) extracted from a single pixel at the positions/components labelled in Fig. 5. For each position, the left-hand panel shows SiO (5−4) (solid black line) and SO 6(5)−5(4) (dashed red line) and the right-hand panel shows ^{12}CO (2−1) (solid blue line) and H_2CO 3(0, 3)−2(0, 2) (dashed green line). Panels labelled 1–3 represent emission extracted from positions along A1 and the vertical dashed black line represents the v_{LSR} of C-MM3 at 7.1 km s^{-1}. Panels labelled 4–8 represent emission extracted from positions along A2 and the vertical black dashed line represents the v_{LSR} of C-MM12 of 8.9 km s^{-1}. Panels with a number 9 or greater represent emission extracted from positions, where SiO emission is present but not obviously associated with an outflow. The H_2CO 3(0, 3)−2(0, 2) emission has been scaled up by a factor of 2 in all spectra. The horizontal black dashed lines are the rms values from the line free channels.

was initially observed to the west of IRS1 in the direction of the ridge feature by Haschick, Menten & Baan (1990). More recently, Slysh & Kalenskii (2009) identified three 44 GHz maser spots with the VLA (resolution 0.15 arcsec) that coincide spatially with the ridge (positions shown in Fig. 8). The strongest of the three 44 GHz maser spots is coincident with the position of the strongest 229 GHz candidate maser emission. Furthermore, the 229/230 GHz line ratio is found to be >15 at the positions of all three 44 GHz maser spots. The v_{LSR} velocity of the 229 GHz emission at the positions of the three 44 GHz maser spots is 8.53, 8.68, and 8.48 km s^{-1}, respectively (for increasing declination in Fig. 8), within ∼1 km s^{-1} of the 44 GHz v_{LSR} measurements from Slysh & Kalenskii (2009), of 7.22, 7.59, and 7.72 km s^{-1}. The coincidence of the class I 44 GHz CH_3OH maser spots with the 229.759 GHz emission in the ridge,

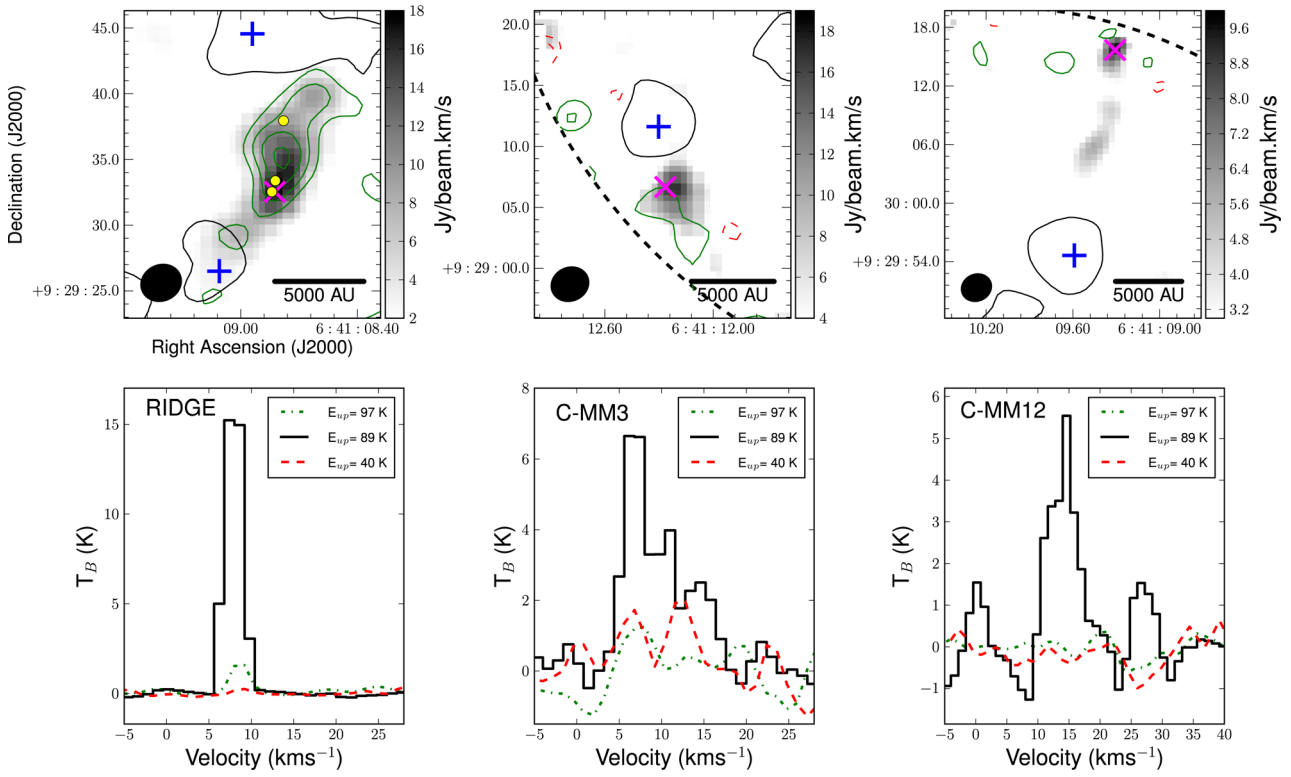

Figure 8. Top: zoom views of integrated intensity maps, corrected for the primary beam response, of CH_3OH 8(−1, 8)−7(0, 7) E (229.759 GHz, grey-scale), CH_3OH 8(0, 8)−7(1, 6) E (220.078 GHz, solid green contours) and CH_3OH 3(−2, 2)−4(−1, 4) E (230.027 GHz, dashed red contours) towards the ridge feature and the redshifted outflow lobes from C-MM3 and C-MM12. The integrated velocity ranges are the same as in Fig. 4. Contour levels: CH_3OH 8(0, 8)−7(1,6) E (220.078 GHz): 3σ, 6σ, 9σ, 12σ, for 1σ values of 0.2, 0.6, and 0.6 Jy beam^{-1} km s^{-1} towards the ridge, C-MM3 and C-MM12, respectively. CH_3OH 3(−2, 2)−4(−1, 4) E (230.027 GHz): 3σ, 5σ for 1σ values of 0.2, 0.4, and 0.5 Jy beam^{-1} km s^{-1} towards the ridge, C-MM3 and C-MM12, respectively. The synthesized beam is shown at lower left in each panel. The blue pluses (+) mark the positions of the millimetre continuum peaks; the solid black line is the 3σ contour of the 1.3 mm continuum emission. The thick dashed line in the C-MM3 and C-MM12 images is the 10 per cent level of the primary beam response. The yellow circles show the positions of the three 44 GHz CH_3OH maser spots detected by Slysh & Kalenskii (2009). Bottom: spectra of the three CH_3OH transitions. The spectra are extracted at the positions of peak CH_3OH 8(−1, 8)−7(0, 7) E (229.759 GHz) emission towards the ridge and the outflows of C-MM3 and C-MM12. These positions are marked by magenta crosses (x) (see also Table 5).

Table 5. Methanol line fits for candidate 229.759 GHz CH_3OH masers in NGC 2264-C.

Species	Transition	ν (GHz)	E_{upper} (K)	RA (J2000)	Dec. (J2000)	Fitted line parameters: Intensity[a] (Jy beam^{-1})	V_{centre}[a] (km s^{-1})	Width[a] km s^{-1}	$\int S\,dv$[a] Jy beam^{-1} km s^{-1}
					Ridge				
CH_3OH	8(0, 8)−7(1, 6) E	220.078	96.6	06 41 08.8	+09 29 32.5	0.66 (0.03)	8.63 (0.04)	2.29 (0.11)	1.63 (0.10)
CH_3OH	8(−1, 8)−7(0, 7) E	229.759	89.1	06 41 08.8	+09 29 32.5	6.64 (0.14)	8.53 (0.03)	2.45 (0.06)	17.31 (0.58)
CH_3OH	3(−2, 2)−4(−1, 4) E	230.027	39.8	06 41 08.8	+09 29 32.5	<0.14[b]	–	–	–
					C-MM3 outflow				
CH_3OH	8(0, 8)−7(1, 6) E	220.078	96.6	06 41 12.3	+09 29 06.7	<0.55[b]	–	–	–
CH_3OH	8(−1, 8)−7(0, 7) E	229.759	89.1	06 41 12.3	+09 29 06.7	2.24 (0.4)	8.16 (0.58)	5.79 (1.63)	13.84 (4.81)
CH_3OH	3(−2, 2)−4(−1, 4) E	230.027	39.8	06 41 12.3	+09 29 06.7	<0.74[b]	–	–	–
					C-MM12 outflow				
CH_3OH	8(0, 8)−7(1, 6) E	220.078	96.6	06 41 09.3	+09 30 15.7	<0.50[b]	–	–	–
CH_3OH	8(−1, 8)−7(0, 7) E	229.759	89.1	06 41 09.3	+09 30 15.7	1.74 (0.21)	14.70 (0.30)	4.85 (0.70)	8.99 (1.70)
CH_3OH	3(−2, 2)−4(−1, 4) E	230.027	39.8	06 41 09.3	+09 30 15.7	<0.90[b]	–	–	–

Notes. [a]The formal errors from the single Gaussian fits are given in the brackets.
[b]Non-detection. The value given is the 3σ limit, calculated from the rms in the spectrum extracted from the primary-beam-corrected image cube for each position.

both spatially and spectrally, supports the interpretation that the 229.759 GHz transition is masing in the ridge.

4 DISCUSSION

4.1 Nature of the millimetre continuum peaks

4.1.1 Temperature estimates from molecular line emission

Methyl cyanide (CH_3CN) is commonly used to estimate the temperature of warm/hot gas in star-forming regions. Using the method of rotational diagrams and assuming optically thin emission and LTE (e.g. Loren & Mundy 1984; Zhang, Ho & Ohashi 1998), gas temperatures may be derived from the relative integrated intensities of the K-ladder components. Compact CH_3CN emission is identified towards two 1.3 mm continuum peaks, C-MM4 and C-MM5. The highest energy K component detected (at $>3\sigma$) is $K = 3$ towards C-MM4 and $K = 4$ towards C-MM5, with upper-level energies of $E_{\rm upper} = 133$ K and $E_{\rm upper} = 183$ K, respectively. Following Araya et al. (2005), we estimate temperatures of $\sim$90 $\pm$ 48 K and $\sim$108 $\pm$ 36 K and CH_3CN column densities of $\sim 8.6 \times 10^{12}$ cm^{-2} and $\sim 1.6 \times 10^{13}$ cm^{-2} for C-MM4 and C-MM5, respectively, from a linear regression fit (accounting for the uncertainties in the line integrated intensities) to the rotational diagrams, shown in Fig. 9. For C-MM4, the temperature is also estimated by applying the rotation diagram method (e.g. Goldsmith & Langer 1999) to the five detected CH_3OH transitions, which have $E_{\rm upper}$ ranging from $\sim$40–100 K. As noted by Goldsmith & Langer (1999), the optical depth can alter the derived rotation temperature. We iteratively solve for the optical depth and rotational temperature following e.g. Brogan et al. (2009) and Cyganowski et al. (2011). The best fit gives a rotational temperature of $\sim$46 $\pm$ 11 K for C-MM4 (see Fig. 9). We note that both the A and E CH_3OH transitions are included in the rotational diagram analysis.

4.1.2 Mass estimates from the SMA 1.3 mm continuum emission

Thermal emission from dust and free–free emission from ionized gas can both contribute to the observed continuum flux at millimetre wavelengths. To estimate the contribution from ionized gas, we extrapolate the 3.6 cm VLA flux densities from Reipurth et al. (2004) to 1.3 mm, assuming $S_\nu \propto \nu^{-0.1}$. VLA2 (see table 2 from Reipurth et al. 2004) is coincident with the millimetre continuum peak C-MM4, while VLA3 and VLA4 both fall within the 15σ continuum contour level for C-MM5, where VLA4 is coincident with the peak of the millimetre continuum emission. If we extrapolate the 3.6 cm emission from VLA2 for C-MM4, and the total emission from both VLA3 and VLA4 for C-MM5, we find that the estimated ionized contribution is negligible for both C-MM4 and C-MM5 (<1 per cent at 1.3 mm from free–free emission). We thus conclude that the thermal contribution from the dust dominates the emission at 1.3 mm and estimate the gas mass assuming a simple isothermal model of optically thin dust emission,

$$M_{\rm gas} = \frac{R F_\nu D^2}{\kappa_m(\nu) B_\nu(T_{\rm d})}, \quad (1)$$

where R is the gas to dust mass ratio (assumed to be 100), F_ν is the flux density, D is the distance to the region, $\kappa_m(\nu)$ is the dust opacity, $B_\nu(T_{\rm d})$ is the Planck function and $T_{\rm d}$ is the (assumed) dust temperature. We adopt $\kappa_m = 1.0$ cm^{2}g^{-1} at 1.3 mm, for grains with ice mantles in high-density regions (10^8 cm^{-3}; Ossenkopf & Henning 1994).

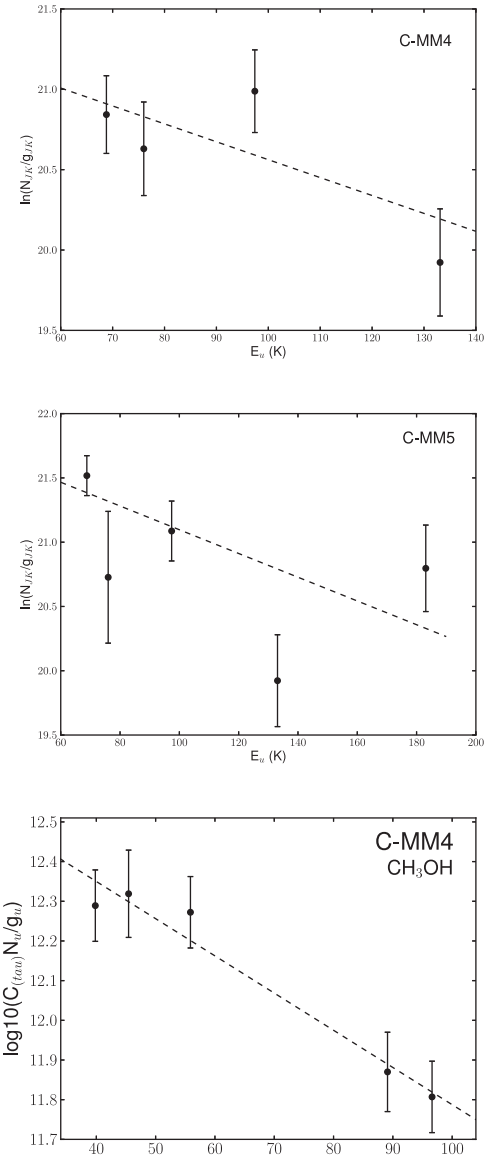

Figure 9. Rotation diagrams for CH_3CN $J = 12_K - 11_K$ observed towards the continuum peaks of CMM4 and C-MM5 (top two panels) and for CH_3OH towards the continuum peak of C-MM4 (bottom panel). The CH_3OH rotation diagram has been corrected for optical depth (Section 4.1.1).

Table 6 presents mass estimates for a range of assumed dust temperatures based on greybody fits to the large-scale dust emission (Ward-Thompson et al. 2000). Two temperature components – of 17 K and 38 K – were required to fit the SED (Ward-Thompson et al. 2000), and we adopt these as lower- and upper-limit temperatures for our mass estimates. We adopt this approach because, for the majority of the dust continuum sources (C-MM4 and C-MM5 excepted, Section 4.1.1), gas temperatures cannot be estimated from our SMA data. For C-MM4 and C-MM5, Table 6 also presents mass estimates assuming $T_{\rm dust} = T_{\rm gas}$ and the gas temperatures from Section 4.1.1. We note that the dust temperatures at the scales probed by our SMA observations are likely to be higher than those measured by Ward-Thompson et al. (2000) from single-dish data. As a result, the mass estimates obtained assuming the single-dish dust temperatures (which range from $\sim$0.1 to 7 $M_\odot$) are likely upper limits for the SMA cores.

Table 6. Mass estimates for 1.3 mm continuum sources in NGC 2264-C.

Source	Mass 17 K ($M_\odot$)	Mass 38 K ($M_\odot$)	Mass[a] CH_3CN ($M_\odot$)	Mass[b] CH_3OH ($M_\odot$)
C-MM3	5.4	2.0	–	–
C-MM4	6.8	2.5	$1.0^{+1.3}_{-0.4}$	$2.0^{+0.8}_{-0.4}$
C-MM5	1.8	0.7	$0.21^{+0.1}_{-0.1}$	–
C-MM10	1.6	0.6	–	–
C-MM12	3.8	1.4	–	–
C-MM13	0.7	0.3	–	–
SMA1	0.3	0.1	–	–
SMA2	0.4	0.1	–	–
SMA3	0.4	0.1	–	–
SMA4	0.5	0.2	–	–

Notes. [a]Mass estimated using $T_{gas} = T_{dust}$ and the rotation temperature estimate for CH_3CN (Section 4.1.1).
[b]Mass estimated using $T_{gas} = T_{dust}$ and the rotation temperature estimate for CH_3OH (Section 4.1.1).

Despite the (considerable) uncertainties introduced by the dust temperature, C-MM3, C-MM4, and C-MM12 appear as the three most massive 1.3 mm continuum sources: they are the only sources with estimated masses $>1\,M_\odot$ for all assumed temperatures. Notably, the outflow-driving sources C-MM3 and C-MM12 are both spatially compact, in contrast to C-MM4 (Table 1, Fig. 2). Furthermore, unlike C-MM4, both C-MM3 and C-MM12 are individual separate structures with no indication of further substructure. We note that the mass estimate for C-MM5 in Table 6 encompasses both C-MM5 and C-MM5b, and so may be an overestimate for the mass of C-MM5 alone. The newly identified millimetre continuum sources (e.g. SMA1, SMA2, SMA3, and SMA4) have the lowest estimated masses, $\leq 0.5\,M_\odot$. The 5σ sensitivity limit of the observations corresponds to $\sim 0.14\,M_\odot$ and $\sim 0.05\,M_\odot$ for 17 and 38 K, respectively.

4.1.3 *Notes on individual millimetre continuum sources*

The 1.3 mm continuum sources in NGC 2264-C display a wide range of associated molecular line emission in our SMA data. C-MM4 exhibits the richest line emission, with a hot-core-like spectrum, while C-MM3, C-MM13, and SMA-4 are not associated with any molecular line emission that can be directly associated with the millimetre continuum cores (as opposed to e.g. outflow emission, Section 3.2.1). The presence/absence and relative strengths of molecular lines detected in wide-bandwidth interferometric observations may be indicative of evolutionary state; however, there is a degeneracy with core mass (e.g. Zhang et al. 2007; Galván-Madrid et al. 2010; Cyganowski et al. 2012; Immer et al. 2014; Wang et al. 2014). We discuss the nature of the individual 1.3 mm continuum sources in NGC 2264-C, with reference to their molecular line emission (or lack thereof) and their 24/70 μm properties (also indicative of evolutionary state; e.g. Battersby et al. 2011), below.

CMM-3: The molecular line emission observed in the vicinity of CMM-3 with the SMA is associated with the outflow driven by this millimetre continuum core (Section 3.2.2; see also Saruwatari et al. 2011). No compact molecular line emission is detected coincident with the millimetre continuum source; this may, however, be due to sensitivity limitations, as CMM-3 is located at the ∼20 per cent power level of our SMA primary beam. No *Herschel* PACS 70 μm or *Spitzer* MIPSGAL 24 μm emission is detected towards CMM-3,[9] indicating that CMM-3 is likely young; the detection of N_2H^+ (1−0) (Peretto et al. 2007) and the enhancement of SCUBA 450 μm emission are also consistent with youth.

C-MM3 is one of the most massive cores in NGC 2264-C (based on our SMA mass estimates, Section 4.1.2). Our SMA observations recover ∼30 per cent of the 1.3 mm single-dish flux density (e.g. Ward-Thompson et al. 2000; Peretto et al. 2006). We note that our mass estimate for C-MM3 is lower than those of Saruwatari et al. (2011),[10] Peretto et al. (2006), Peretto et al. (2007), and Ward-Thompson et al. (2000), due to differences in spatial filtering (when comparing interferometric and single-dish data), and in assumed opacities and dust temperatures (along with the recently revised distance to the region). If we adopt the temperature, opacity (scaled to 1.3mm), and distance assumed by Peretto et al. (2007), we obtain a mass estimate from our SMA data comparable to their estimate based on their PdBI observations. Interestingly, Peretto et al. (2007) suggest that C-MM3 harbours a disc of mass 1.1 $M_\odot$, which would be a substantial fraction of our estimated mass of ∼2–5 $M_\odot$ (Table 6).

C-MM4, the most molecular line rich core, displays a hot core-like spectrum. Compact molecular line emission with E_{upper} temperatures of 55–133 K from typical hot core tracers such as OCS, CH_3CN, CH_3OH, and HC_3N is coincident with the continuum peak on scales of ∼0.01 pc. Fig. 10 displays the line profiles for all transitions observed towards the continuum peak of C-MM4. In addition to the compact emission, several transitions tracing more diffuse emission are also identified such as N_2H^+ (1−0) (Peretto et al. 2007), DCN, and $C^{18}O$. No clear outflow is identified in the molecular line emission towards this core. The FIR 70 μm *Herschel* emission (see Fig. 1) is dominated by the bright infrared source AFGL 989-IRS1 in this region. However, at the continuum peak of C-MM4 the 70 μm flux is approximately 50 per cent brighter than at other positions at similar radii from IRS1, suggesting that C-MM4 is contributing to the 70 μm flux. In addition, 3.6 cm emission (VLA2 in Reipurth et al. 2004) is detected coincident with the continuum peak. No 24 μm emission is detected towards the continuum peak of C-MM4.

We find a 1.3 mm flux density of 496 mJy for this source, which recovers approximately half of the single-dish flux (e.g. Ward-Thompson et al. 2000; Peretto et al. 2006). Peretto et al. (2006) estimate a mass of 35 $M_\odot$ from their single-dish observations, which is comparable to their single-dish mass estimate for C-MM3 of ∼40 $M_\odot$. However, the morphology of C-MM4 is noticeably more extended than C-MM3. The molecular line emission also suggests that at least the central region of C-MM4 is likely warmer than C-MM3. Our mass estimates for C-MM4 using the CH_3CN and CH_3OH rotational temperatures are ∼1–2 $M_\odot$. These results indicate C-MM4 is potentially lower in mass and more evolved than C-MM3.

C-MM5 coincides with the position of the IR-bright B2 2000 $L_\odot$ star AFGL 989-IRS1. This well-studied source dominates both the 24 and 70 μm emission in this region. We detect comparatively little molecular line emission towards this continuum peak. The molecular line emission detected is shown in Fig. 11. Furthermore,

[9] Strong 70, 24, and 2.2 μm emission are observed to the south-east of C-MM3. This emission is not directly associated with C-MM3, but is from a separate star with a weak, diffuse nebulosity surrounding it.
[10] Our measured flux density for C-MM3 agrees within ∼20 per cent with that reported by Saruwatari et al. (2011) based on SMA observations with similar spatial resolution.

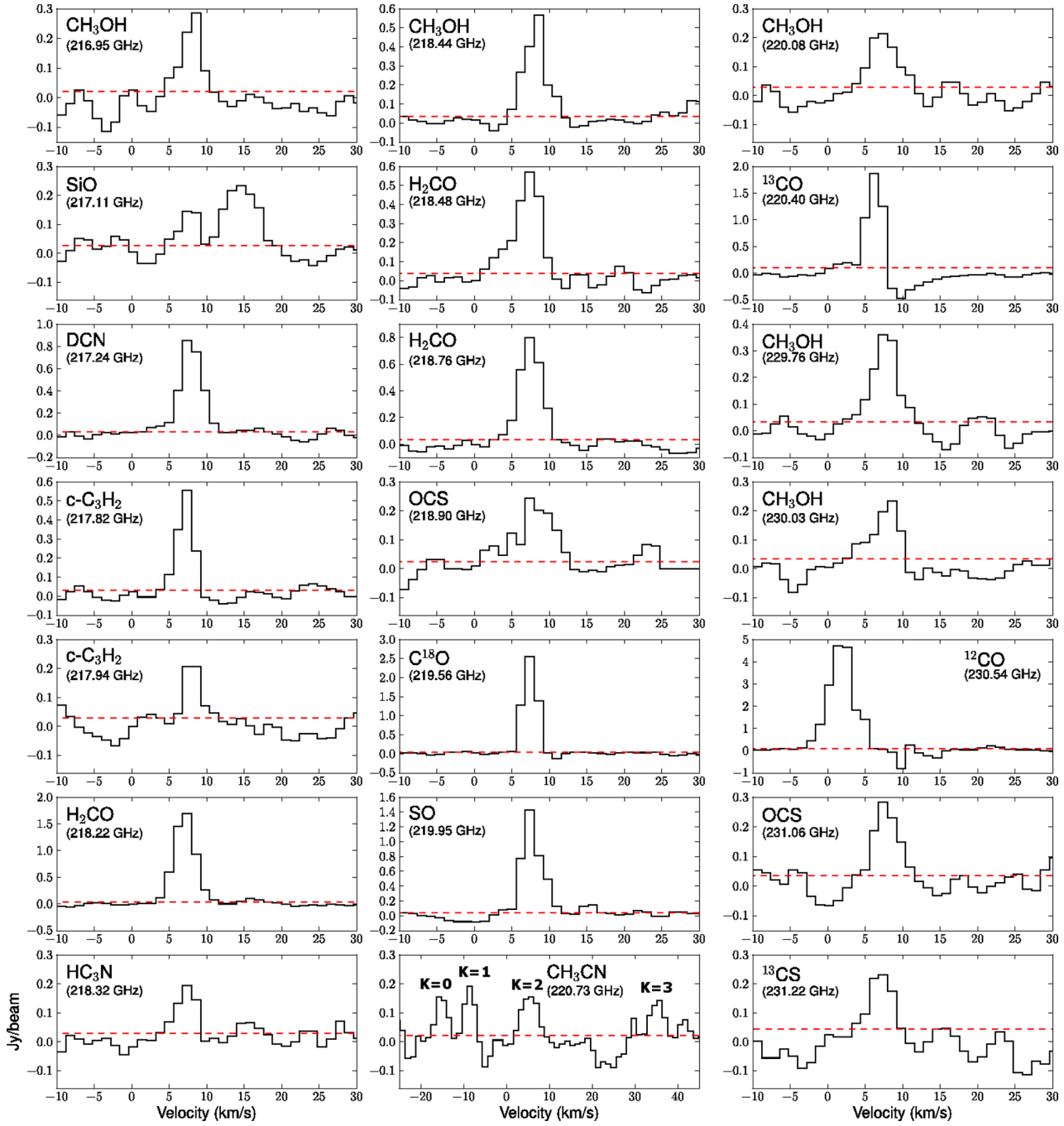

Figure 10. Spectra of transitions detected at the continuum peak of C-MM4, extracted from image cubes corrected for the primary beam response. Each transition detected above 5σ is shown. The CH_3CN ladder is shown in a single panel, centred on the $K = 2$ transition (rest frequency = 220.730 GHz): the velocity range shown includes all K ladder transitions detected at $>3\sigma$ with the transitions labelled in the panel. In each panel, the horizontal red dashed line is the spectral rms noise and the transition and rest frequency are given in the top-left corner.

we find no obvious indication that an outflow is driven by this source in any of the observed molecular transitions, despite the detection of a twisted jet feature at 1.65 and 2.2 μm by Schreyer et al. (1997) to the north-west of C-MM5. This source also drives a dense stellar wind (Bunn, Hoare & Drew 1995) that has excavated a low-density cavity around AFGL 989-IRS1 (Schreyer et al. 2003). That may account for the lack of molecular line emission detected towards this source, if a low-density cavity created by a wind/jet has removed part or all of the outer envelope. While molecular line emission from the lower energy transitions is lacking, compact emission from CH_3CN and HC_3N is coincident with the peak of the continuum emission. Grellmann et al. (2011) have previously identified a disc in this source. As emission from CH_3CN is known to trace discs (e.g. Cesaroni et al. 2014 and references therein), we suggest the emission from CH_3CN and HC_3N may be related to the presence of a disc in AFGL989-IRS1. On the other hand, as C-MM5, unlike C-MM4, does not display a typical hot core-like spectrum, and given CH_3CN has also been previously detected in low-velocity shocks and in outflows (e.g. Csengeri et al. 2011; Bell et al. 2014), the emission in C-MM5 from these compact tracers could also be

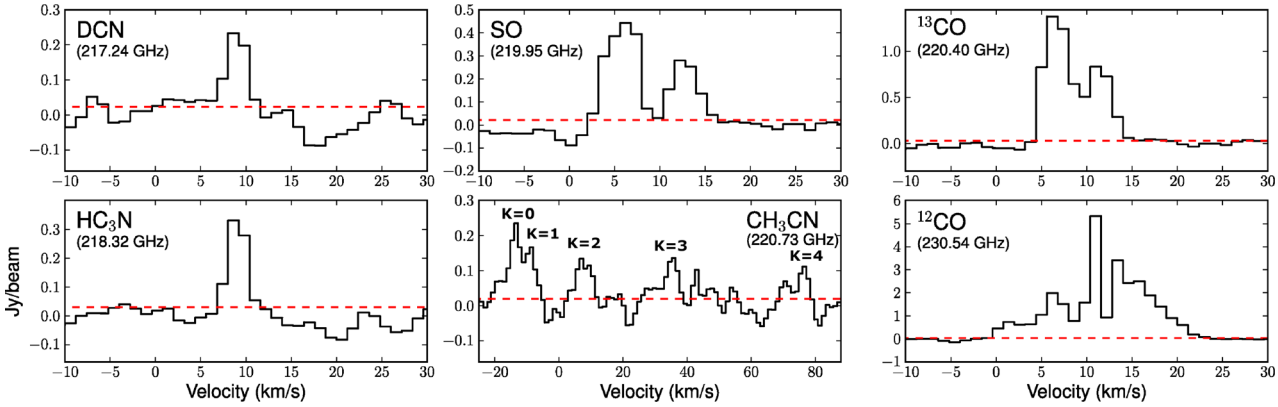

Figure 11. Spectra of transitions detected at the continuum peak of C-MM5, extracted from image cubes corrected for the primary beam response. Each transition detected above 5σ is shown. The CH_3CN ladder is shown in a single panel, centred on the $K = 2$ transition (rest frequency = 220.730 GHz): the velocity range shown includes all K ladder transitions detected at $>3\sigma$ with the transitions labelled in the panel. In each panel, the horizontal red dashed line is the spectral rms noise and the transition and rest frequency are given in the top-left corner.

due to shocks. An additional indication that AFGL 989-IRS1/C-MM5 is comparatively evolved is the detection of 3.6 cm emission (VLA sources 3 and 4; Reipurth et al. 2004).

For C-MM5, our SMA observations only recover ∼25 per cent of the single-dish flux. However, we only consider the 1.3 mm flux density estimated for C-MM5 and not the entire parent structure, which also includes the new detections SMA1 and SMA2. Peretto et al. (2006) estimate a mass of ∼18 $M_\odot$ from their single-dish observations. We estimate a gas mass, using the temperature estimate from CH_3CN, of ∼0.2 $M_\odot$ for C-MM5, which is lower than for C-MM3 or C-MM4. Furthermore, this mass estimate potentially incorporates an additional source, C-MM5b, and so the mass of C-MM5 may be lower still. As discussed in Section 3.1, we suggest C-MM5b is likely a separate source that at the current resolution we are unable to spatially resolve. The presence of the strongest 70, 24, 1.65, and 2.2 μm emission, along with the previous detections of a disc and 3.6 cm radio continuum, suggest that C-MM5 is likely the most evolved source in our field.

C-MM10 displays very little molecular line emission. However, 70 μm emission is observed towards the continuum peak (Fig. 1). This source is notably extended (Fig. 2) compared with the compact morphology of cores such as C-MM3 and C-MM12. Furthermore, only ∼10 per cent of the single-dish flux reported in Peretto et al. (2006) is recovered with the SMA, which may suggest that the bulk of the 1.3 mm emission associated with this source is from an extended region that we currently resolve out. C-MM10 is likely a low-mass source, but its exact nature is unclear.

CMM-12 lacks emission from most typical hot core tracers. Only compact emission from OCS ($E_{upper} = 99.8$ K) is detected towards the continuum peak. The majority of the molecular line emission in the vicinity of this source (such as SiO, H_2CO, and SO) is from the outflow driven by this millimetre continuum core. As emission from OCS has previously been suggested to be tracing the inner regions of the outflow (e.g. Cyganowski et al. 2011), the OCS emission is likely also tracing the outflow, rather than the continuum peak. C-MM12 also lacks any obvious 70 or 24 μm emission. Our estimated mass for this source is 1.4–3.8 $M_\odot$, approximately half of the estimated mass for C-MM3. We recover a notably high proportion of the single-dish flux, ∼90 per cent. The single-dish mass is estimated to be ∼9 $M_\odot$ (Peretto et al. 2006). These results suggest C-MM12 is likely a low/intermediate-mass protostar.

C-MM13 displays one of the most molecular line poor spectra. Furthermore, we find no enhancement of 450, 70, or 24 μm emission towards C-MM13. The $N_2H^+(1-0)$ line, however, displays the strongest emission coincident with this peak (Peretto et al. 2007). Our estimated mass for this source is in the range 0.3–0.7 $M_\odot$, compared with ∼8 $M_\odot$ from Peretto et al. (2007). Scaling our mass assuming the parameters from Peretto et al. (2007), we would still only estimate a mass of ∼2 $M_\odot$ for C-MM13. Furthermore, C-MM13 is not detected in the single-dish observations. These results suggest C-MM13 is a low mass, likely young protostar. However, its nature, as with the continuum peak C-MM10, is unclear.

SMA1, SMA2, SMA3, and SMA4 are all new 1.3 mm detections.[11] None of these newly detected 1.3 mm continuum peaks display enhancements in 450, 70, or 24 μm emission, and only towards SMA4 is there $N_2H^+(1-0)$ emission (Peretto et al. 2007). SMA2 and SMA3 are the most molecular line rich of the four. No emission from the 'compact' tracers (Section 3.2) is detected towards any of these four continuum peaks. The mass estimates are <0.5 $M_\odot$ for all four new detections, for all assumed gas temperatures. Three of the four new detections are nested within a parent tree structure. SMA1 and SMA2 are part of the same parent structure as AFGL 989-IRS1/C-MM5, where SMA1 is spatially coincident with the twisted jet feature to the north of this source, and SMA4 forms part of the same parent structure as C-MM4. Furthermore, Kamezaki et al. (2014) identified an associated water maser coincident with SMA4, and given the association of N_2H^+ and 3.2 mm emission in Peretto et al. (2007) they designate this source as C-MM4S. In addition, they note the association of an X-ray source (FMS2-1269; Flaccomio, Micela & Sciortino 2006) with this continuum peak, suggesting that it is an X-ray emitting class 0 source. SMA3 is the only new mm detection that is found as an independent structure. It is spatially coincident with the southern edge of the ridge feature.

4.2 Nature of the ridge

As noted in Section 3.2.3, a prominent feature in our SMA molecular line observations is the 'ridge'. This feature is detected in all three H_2CO transitions, and three CH_3OH transitions:

[11] SMA4 was marginally detected at 3.2 mm with the PdBI by Peretto et al. (2007), but was not considered as an unambiguous detection.

Table 7. SiO (5−4) and ^{12}CO (2−1) outflow properties.

Outflow[a]	L[b] (arcsec)	v_{max}[c] (km s^{-1})	$\|v_{max} - v_{LSR}\|$ (km s^{-1})	Inclination[d] (Deg)	l_{flow}[e] (corrected) (au)	$\|v_{max} - v_{LSR}\|$[f] (corrected) (km s^{-1})	T_{dyn}[g] (yr)	Integrated[h] flux density (Jy km s^{-1})
				SiO (5−4)				
C-MM3 R1	6	36.8	29.7	45–60	6200–5100	42–60	700–410	21
C-MM3 B1	4	− 19.6	26.7	45–60	4200–3400	38–53	520–300	13
C-MM3 B2	13	− 5.2	12.3	45–60	13600–11000	17–25	3700–2100	6
C-MM12 red lobe	22	32.0	23.0	45–60	23000–18700	32–46	3400–2000	67
C-MM12 blue lobe	22	− 1.6	10.6	45–60	23000–18700	15–22	7300–4200	20
				^{12}CO (2−1)				
C-MM3 R1	6	38.0	30.9	45–60	6200–5100	44–62	680–390	68
C-MM3 B1	3	− 17.2	24.3	45–60	3100–2500	34–49	430–240	30
C-MM3 B2	11	− 5.2	12.3	45–60	11500–9300	17–25	3100–1800	1
C-MM12 red lobe	19	32	23.0	45–60	19800–16200	33–46	2900–1700	179
C-MM12 blue lobe	17	− 2.8	11.8	45–60	17700–14500	17–24	5000–2900	79

Notes. [a]The blueshifted lobe of C-MM3 has been treated as two separate components, B1 and B2. As we do not detect emission from the redshifted R2 component of C-MM3 identified by Saruwatari et al. (2011), all properties for the C-MM3 red lobe are calculated from the R1 component only (see Fig. 5).
[b]Angular distance between the continuum peak and the farthest positional offset for the SiO (5−4) and ^{12}CO emission in arcseconds.
[c]The absolute velocity of the first/last channel in the image cubes (corrected for the primary beam response) where emission is detected above 3 σ.
[d]The outflow length, maximum velocity, and dynamical time-scale are influenced by the assumed inclination. Saruwatari et al. (2011) assume an inclination of 60° for C-MM3; as we are unable to determine the inclination, we report outflow properties assuming both an inclination of 45° and 60° from the line of sight.
[e]Calculated from the maximum lobe length and corrected for inclination using $l_{flow(corrected)} = l_{flow}/\sin(i)$; converted to au assuming a distance of 738 pc (Kamezaki et al. 2014).
[f]Calculated from $|v_{max} - v_{LSR}|$ corrected for inclination using $(|v_{max} - v_{LSR}|)/\cos(i)$.
[g]Dynamical time-scale calculated using $T_{dyn} = l_{flow(corrected)}/v_{max(corrected)}$.
[h]Total integrated intensity calculated from images corrected for the primary beam response. For SiO, the emission is integrated from the v_{LSR} (7.2 and 8.9 km s^{-1} for C-MM3 and C-MM12, respectively) to the maximum velocity of each lobe. For ^{12}CO (2−1), the emission is integrated over the velocity ranges stated in Table 8, which exclude emission at low velocities close tothe systemic velocity due to confusion.

CH_3OH 4(2, 2)−3(1, 2) (218.440 GHz), CH_3OH 8(0, 8)−7(1, 6) E (220.078 GHz) and CH_3OH 8(−1, 8)−7(0, 7) E (229.759 GHz). In all of these transitions, the ridge feature displays the strongest emission compared with any other location in the region. The emission from these transitions typically extends over a spatial scale of ∼15 000 au in length (taken along the PA = 150 deg), with a perpendicular width of ∼2000–5000 au. We note that along the length of the ridge the width varies and is not always resolved by our beam. The ridge is not clearly associated with a millimetre continuum peak: only the southern edge of the ridge spatially coincides with the continuum peak SMA3. At this position, we find compact redshifted emission traced by SiO, SO and H_2CO in the SHV regime, and ^{12}CO emission in the IHV regime. While no blueshifted counterpart is found towards the ridge, we do find a possible blueshifted component traced by ^{12}CO coincident with C-MM4. Thus, the redshifted emission at the southern edge of the ridge may be from an outflow running north-west–south-east between C-MM4 and SMA3 where the associated driving source is not obvious.

The ratio of the 229 and 230 GHz CH_3OH lines (discussed in Section 3.2.3) is an indication of the non-thermal nature of the 229 GHz emission towards the ridge. In addition, Slysh & Kalenskii (2009) detect 44 GHz class I CH_3OH masers towards the ridge. While class I CH_3OH masers have typically been associated with outflows (e.g. Plambeck & Menten 1990; Kurtz, Hofner & Álvarez 2004; Cyganowski et al. 2009), Voronkov et al. (2010, 2014) suggest that class I masers can also be excited in the shocks formed by expanding H II regions. The maser emission in the ridge could therefore be attributable to shocks from an outflow (although we do not detect a clear powering source) or from a wind impacting the ambient medium. As the ridge is located at the edge of a low-density cavity driven by AFGL 989-IRS1 (e.g. Schreyer et al. 2003; Nakano, Sugitani & Morita 2003), the maser emission in the ridge could be a result of the dense stellar wind from IRS1 (Bunn et al. 1995) colliding with a region of high-density ambient material.

4.3 Outflow properties

We identify two unambiguous, high velocity bipolar outflows, traced by SiO, SO, H_2CO, CH_3OH, and ^{12}CO emission, driven by C-MM3 and C-MM12. In Table 7, we present the outflow parameters (e.g. outflow length, maximum velocity, and dynamical time-scale) estimated from both the SiO (5−4) and ^{12}CO (2−1) emission for the two clearly defined bipolar outflows. The dynamical time-scale is given as $T_{dyn} = l_{flow}/(|v_{max} - v_{LSR}|)$, where l_{flow} is the observed maximum outflow length on the sky, and v_{max} is the absolute velocity of the maximum/minimum channel in the image cube with a 3σ detection. The inclination (i) of the outflow to the line of sight affects the estimates of both the outflow length ($l_{flow(corrected)} = l_{flow}/\sin(i)$) and the maximum velocity with respect to the v_{LSR} e.g. $((|v_{max} - v_{LSR}|)/\cos(i))$, and thus the dynamical time-scale. We present estimates for inclinations of both 45 and 60 deg in Table 7. Towards C-MM3, we treat the two spatially separated blueshifted components, B1 and B2 (identified by Saruwatari et al. 2011, see Fig. 5), independently and provide dynamical time-scale estimates for both. For the blueshifted component B1 and the redshifted lobe, we find similar maximum lengths, and absolute velocity estimates from the SiO (5−4) emission. We note that towards the redshifted lobe, only emission from component R1 is detected. Saruwatari et al. (2011) also identified a second redshifted component R2 (see their Figs 2 and 5 presented here); however, R2 is outside of the 10 per cent power level of our primary beam. Thus, we only use emission from R1 to estimate the outflow parameters for the redshifted lobe of C-MM3.

Table 8. Derived outflow properties estimated from the ^{12}CO (2−1) emission.

Outflow	Inclination[a] (Deg)	Δv[b] (km s^{-1})	M_{out} (10^{-3} M$_\odot$)	P_{out}[c] (M$_\odot$ km s^{-1})	E_{out}[c] (erg) ($\times 10^{43}$)	$\dot{M}_{out}$[c] M$_\odot$ yr^{-1}) ($\times 10^{-6}$)	$\dot{P}_{out}$[c] (M$_\odot$ km s^{-} yr^{-1}) ($\times 10^{-5}$)
C-MM3 red lobe[d]	45–60	15.2–38.0	2.5	0.06–0.08	1.53–3.0	3.6–6.4	8.8–20.5
C-MM3 blue lobe[d]	45–60	− 17.2–0.8	1.1	0.02–0.03	0.5–1.0	2.6–4.6	4.6–12.5
C-MM12 red lobe	45–60	16.4–32.0	6.5	0.12–0.17	2.5–4.9	2.2–3.8	4.1–10.0
C-MM12 blue lobe	45–60	− 2.8–0.8	2.8	0.04–0.05	0.5–0.9	0.6–1.0	0.8–1.7

Notes. [a]Inclination from line of sight: the outflow properties are estimated for assumed inclinations of 45° and 60°.
[b]The velocity range used to estimate the outflow properties, taken from the absolute velocities in the image cube, the maximum velocity is taken from the velocity of the first/last channel in the image cubes (corrected for the primary beam response) where emission is detected above 3 σ.
[c]Values are calculated from the dynamical time-scale estimates from the ^{12}CO (2−1) emission presented in Table 7.
[d]The values presented for the blueshifted outflow lobe of C-MM3 are the sum of the B1 and B2 outflow components shown in Fig. 5; $\dot{M}_{out}$ and $\dot{P}_{out}$ are calculated from the dynamical time-scale of the B1 component. The R2 component reported by Saruwatari et al. (2011) is not detected in our observations so all values for the redshifted lobe are derived only from the R1 component (see Fig. 5).

The dynamical time-scales estimated from SiO (5−4) are ∼300–500 yr and ∼400–700 yr for B1 and the redshifted lobe of C-MM3, respectively. Additionally, we find similar estimates of the outflow properties from the ^{12}CO (2−1) emission. We note that the blueshifted emission from B1 is at a slightly lower absolute maximum velocity than the redshifted emission, and is approximately 3 and 6 km s^{-1} slower for SiO (5−4) and ^{12}CO (2−1), respectively. At the position of the more northern blueshifted component B2, an even lower absolute maximum velocity with respect to the v_{LSR} of ∼12 km s^{-1} and dynamical time-scale estimate of ∼2000–3500 yr is obtained for both the SiO (5−4) and ^{12}CO (2−1) emission. In both tracers, B2 is approximately an order of magnitude older compared with either the higher velocity blueshifted component B1 or the redshifted lobe. We suggest the outflow driven by C-MM3 may be impacting with dense material at this position, which is causing it to slow further from the central core. In addition to the blueshifted components, B1 and B2, Saruwatari et al. (2011) also identified a second weaker, lower velocity redshifted component, R2, which is similarly offset and has a similar maximum velocity offset with respect to the v_{LSR} as B2. If both the red and blueshifted lobes are similarly slowed due to an impact with ambient material, then C-MM3 may be centrally located in a dense envelope.

The red- and blueshifted outflow lobes driven by C-MM12 have a similar maximum length on the sky of ∼20 arcsec (∼15 000 au) in both the SiO (5−4) and ^{12}CO (2−1) emission. However, the blueshifted lobe has a considerably lower maximum velocity with respect to the v_{LSR} compared with the redshifted lobe in both tracers. This results in noticeably longer dynamical time-scale estimates for the blueshifted outflow lobe, which may indicate that the blueshifted lobe is slowed, possibly due to an impact with ambient material. Moreover, the integrated SiO (5−4) flux density of the lower velocity blueshifted lobe is significantly lower than the integrated SiO (5−4) flux density towards the higher velocity, redshifted lobe (see Table 7). This result again points towards SiO (5−4) being a more effective tracer of high-velocity shocks.

Assuming the ^{12}CO (2−1) emission is optically thin at high velocities, we follow the procedure outlined in Cyganowski et al. (2011, and references therein) and estimate the outflow mass from the ^{12}CO (2−1) emission using

$$M_{out} = \frac{1.186 \times 10^{-4}\, Q(T_{ex})\, e^{\frac{E_{upper}}{T_{ex}}}\, D^2 \int S_\nu \mathrm{d}\nu}{\nu^3 \mu^2 S \chi}, \quad (2)$$

where M_{out} is the outflow gas mass given in units of $M_\odot$, T_{ex} is the excitation temperature in Kelvin, $Q(T_{ex})$ is the partition function, ν is the frequency in GHz, χ is the abundance relative to H_2, D is the distance to NGC 2264-C in kpc, and S_ν is the ^{12}CO (2−1) flux in Jy. We do not estimate an outflow mass using the SiO emission due to the uncertainty in the SiO to H_2 abundance ratio. If we adopt the same excitation temperature used by Maury et al. (2009) of 20 K, then $Q(T_{ex})$ is estimated to be 7.56 following Mangum & Shirley (2015)[12] for ^{12}CO. We use a standard value of 10^{-4} for the ^{12}CO to H_2 abundance ratio (Frerking, Langer & Wilson 1982). Following the procedure from Qiu et al. (2009), we estimate the outflow momentum and energy from

$$P_{out} = \sum M_{out}(\Delta v)\Delta v \quad (3)$$

and

$$E_{out} = \frac{1}{2}\sum M_{out}(\Delta v)(\Delta v)^2, \quad (4)$$

where $M_{out}(\Delta v)$ is the outflow mass calculated for a given channel of velocity $\Delta v = |v_{channel} - v_{LSR}|$. In Table 8, we provide estimates of M_{out}, P_{out}, and E_{out} for the red- and blueshifted outflow lobes driven by C-MM3 and C-MM12. The values presented for the blueshifted lobe driven by C-MM3 are taken from the total contribution of the B1 and B2 components. For the redshifted lobe, we do not detect emission from R2 and only emission from the R1 component is included in the derived outflow properties. We only consider the high-velocity gas in the estimates of the outflow mass, momentum, and energy and the respective velocity ranges assumed for each lobe are presented in Table 8. In addition, we estimate the mass and momentum outflow rates, $\dot{M}_{out} = M_{out}/t_{dyn}$ and $\dot{P}_{out} = P_{out}/t_{dyn}$, using the dynamical time-scale estimates presented in Table 7. Given that the main blueshifted component, B1, contains more than 90 per cent of the total mass contained in both the B1 and B2 components, we use the dynamical time-scale estimated for B1 to derive estimates of the mass and momentum outflow rates presented in Table 8 for C-MM3. All properties are corrected for inclinations of $i = 45°$ and 60°. The estimated outflow masses for the blue- and redshifted lobes are 1.1 × 10 and 2.5 × 10^{-3} M$_\odot$, respectively, compared to previous outflow mass estimates using ^{12}CO (2−1) by Saruwatari et al. (2011) of 1.6 × 10^{-3} and 2.6 × 10^{-3} M$_\odot$ for the blue- and redshifted lobes, respectively. The lower estimates found in this work may be due the R2 component in our data being located outside of the 10 per cent power level and thus not

[12] Assuming a rotational constant estimated using Splatalogue (http://www.splatalogue.net/), Müller et al. (2005).

included in the mass estimate and in the blueshifted lobe we detect ^{12}CO (2−1) emission down to an absolute velocity of −17.2 km s^{-1} compared with −20 km s^{-1} in Saruwatari et al. (2011).

We find that the outflow driven by C-MM12 is more than twice as massive and contains approximately twice the momentum and energy compared with the outflow from C-MM3. However, the mass and momentum outflow rates estimated for the outflow driven by C-MM3 are more than double those found towards the outflow from C-MM12. Given these results and the fact that the dynamical time is found to be shorter for C-MM3 compared with C-MM12, we speculate that the more massive core C-MM3 may be driving a younger, less massive outflow compared with the lower mass core C-MM12. We note, however, that we have not fully accounted for possible inclination differences between the outflows which can significantly affect the estimation of the dynamical time-scale. In both outflows we observe an apparent asymmetry between the outflow properties of the higher velocity, redshifted, and lower velocity, blueshifted, outflow lobes. In both cases, the redshifted lobes are twice as massive and contain approximately three times more momentum and energy compared with their respective blueshifted lobes.

4.3.1 Comparison with previous single-dish observations of outflows in NGC 2264-C

One of our main goals was to unambiguously identify the driving sources of the several high-velocity outflow lobes observed in NGC 2264-C by Maury et al. (2009) using single dish ^{12}CO (2−1) at ∼11 arcsec resolution, through higher resolution SMA observations (∼3 arcsec). Maury et al. (2009) identified five outflow lobes (F1, F2, F5, F7, F11; see their fig. 2) in our SMA field of view, suggesting either C-MM3 or C-MM13 as the most likely candidate to be driving the collimated red- (to the north) and blueshifted (to the south) outflow lobes F1 and F2, respectively. While we identify no obvious outflow emission, from any of our high-velocity outflow tracers, along either F1 or F2, we do identify high-velocity compact bipolar outflow driven by C-MM3. However, in contrast to the direction of the red- and blueshifted F1 and F2 lobes shown in Maury et al. (2009, north to south, respectively), we observe the redshifted lobe of C-MM3 to the south and the blueshifted lobe to the north (i.e. in the opposite direction). Similarly, in our single-dish SiO (8−7) observation towards C-MM3 (see Fig. 5) the red- and blueshifted emission is observed to the south and north of C-MM3, respectively. These results suggest neither C-MM3 nor C-MM13 is driving the F1 and F2 lobes observed by Maury et al. (2009). They do find an extended, poorly collimated redshifted lobe (F11) to the south of C-MM3. Thus, the redshifted high-velocity outflow from C-MM3 may then be contributing to the redshifted emission from F11. However, F11 is significantly extended compared with the compact redshifted emission we observe towards C-MM3.

The red and blueshifted lobes F7 and F5 extend over several continuum peaks at the lower spatial resolution of the single-dish ^{12}CO observations (see fig. 2; Maury et al. 2009), and it is not obvious which continuum peak(s) are responsible for the emission. With the higher spatial resolution provided by the SMA, we now identify a collimated bipolar outflow driven by C-MM12. Thus, we can associate the lobes F7 and F5 to the outflow driven by C-MM12. Furthermore, as previously mentioned, the fact that our SMA SiO data recover (and resolve) both of the SiO outflows identified with the JCMT is strong evidence that the SMA is not 'missing' any large-scale active outflows.

We estimate outflow masses for the blue- and redshifted lobes driven by C-MM12 of 2.8 × 10^{-3} and 6.5 × 10^{-3} M$_\odot$, respectively, compared to the minimum[13] mass estimates from Maury et al. (2009) of 0.9 × 10^{-2} and 6.0 × 10^{-2} M$_\odot$ for the blue- (F5) and redshifted (F7) outflow lobes, respectively. Thus, we only recover ∼10 and ∼30 per cent of the mass of the red and blueshifted lobes F7 and F5, respectively. However, we have only included redshifted emission situated to the north of C-MM12 and do not include redshifted emission to the south of C-MM12. As shown previously, to the south of C-MM12 there is redshifted emission running from north-west to south-east that may be from another potential outflow axis (components 9 to 11, see Figs 5 and 6), which at the lower spatial resolution is blended with the redshifted emission associated with the outflow driven by C-MM12. Furthermore, we integrate both the red- and blueshifted emission over a smaller velocity range compared with Maury et al. (2009). If we now include the redshifted emission to the south of C-MM12 and extend the velocity ranges, we now estimate a mass of ∼20 × 10^{-3} M$_\odot$ which is ∼30 per cent of the mass estimated by Maury et al. (2009) and a similar blueshifted estimate as previously found. Our beam size is ∼4 times greater than Maury et al. (2009), thus the difference in mass estimates is likely due in part to spatial filtering, but also due to the ability to more accurately separate emission not directly associated with the outflow at higher resolution.

4.3.2 Relative evolutionary state

The two dominant bipolar outflows are being driven by the IR-dark, compact, millimetre bright, and potentially youngest sources, C-MM3 and C-MM12. The lack of 70 and 24 μm emission towards either source and the associated outflow emission indicates that both of these sources are likely at a very early stage of evolution. In comparison, no obvious active outflow emission from SiO (8−7), SiO (5−4), or high velocity ^{12}CO (2−1) is associated with C-MM5, which is coincident with the most evolved star in the region, AFGL989-IRS1, a 9.5 M$_\odot$ star. Thus, the presence of an SiO outflow appears to decline with evolution for this region. Klaassen, Testi & Beuther (2012) found an opposite trend in their survey of SiO (8−7) emission towards massive star-forming regions, finding an increase of the SiO luminosity with evolution, which was also weakly observed by Leurini et al. (2014) in their sample. Davies et al. (2011) predict the lifetime for YSOs to dramatically drop for sources with a bolometric luminosity of ∼10$^{5.5}$ L$_\odot$ or greater. The typical bolometric luminosity of the sources in Klaassen et al. (2012) is of the order of 10^4–10^5 L$_\odot$, with several objects at a few ×10^5 L$_\odot$. In comparison, AFGL989-IRS1 has a bolometric luminosity of ∼10^3 L$_\odot$. Thus, it is likely that some possible compact H II regions in Klaassen et al. (2012) will be the same age or possibly younger than the most evolved source in our region, AFGL 989-IRS1, and so the presence of SiO may decline with age, as seen by Sánchez-Monge et al. (2013), consistent with the low-mass scenario of the jet declining with age. In addition, the most evolved sources observed by Klaassen et al. (2012) and Leurini et al. (2014) may also host companion younger objects given the coarse angular resolution of the data sets (JCMT 15 arcsec, and APEX 18 arcsec, respectively).

[13] Maury et al. (2009) estimate both a minimum and maximum mass for each lobe depending on velocity range used, see section 4 of Maury et al. (2009) for a detailed explanation.

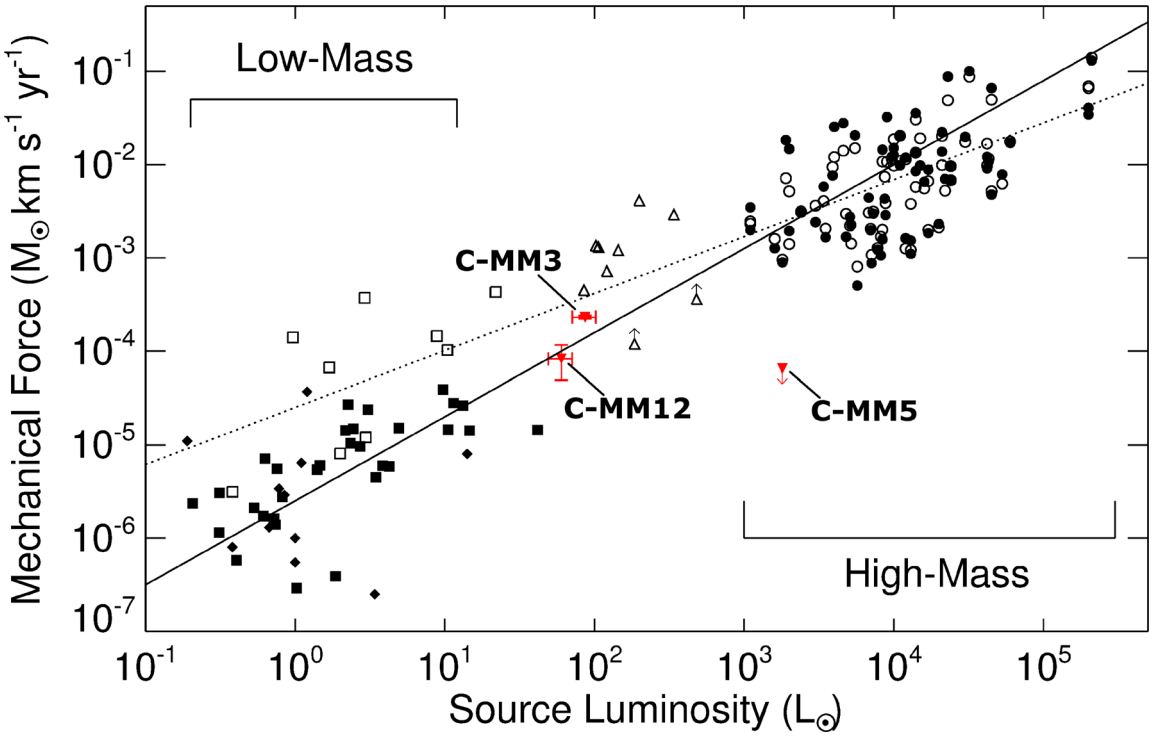

Figure 12. Outflow force versus bolometric luminosity adapted from fig. 7 of Maud et al. (2015). The filled and open circles are from Maud et al. (2015) and represent outflow forces calculated using a fixed dynamical time-scale ($t_{\rm dyn} = R_{\rm max}/v_{\rm max}$, the same method adopted in this paper) and those summed from maps where a position-variable $t_{\rm dyn}(x, y)$ is used, respectively (see Maud et al. 2015 for more details). The filled diamonds are the ∼ class I sources from van der Marel et al. (2013), the open and filled squares are class 0 and class I low-mass outflow sources from Bontemps et al. (1996), and the open triangles are intermediate-mass class 0 analogues from Duarte-Cabral et al. (2013). The red inverted triangles represent C-MM3, C-MM12, and the upper limit of the estimated force for AFGL989-IRS1/C-MM5, as labelled. The error bars on the outflow force represent the maximum and minimum values (summing both the red- and blueshifted components) estimated for inclinations of 45 and 60 deg, with the main point representing the average value. The uncertainties on the luminosities for C-MM3 and C-MM12 come from the range in the luminosity estimated from the SED fit for C-MM3, with the position of the marker representing the average. For AFGL989-IRS1/C-MM5 the bolometric luminosity is taken from the RMS survey data base (Lumsden et al. 2013). The black dotted line represents the linear fit from the Maud et al. (2015) sample (open and filled circles) extended to the lower luminosity regime. The black solid line is the linear fit to the class I sources from Bontemps et al. (1996) extended to the high-mass regime.

The IR radiation of NGC 2264-C is dominated by AFGL989-IRS1; however, C-MM3 is sufficiently spatially offset (∼40 arcsec) from this source that it is possible to obtain an estimate of the bolometric luminosity of C-MM3. We employ the online SED fitting tool of Robitaille et al. (2007) to fit an SED for C-MM3, using data at five wavelengths: 70 and 160 μm *Herschel* PACS archival data (ID 1342205056, P.I. F. Motte), 450 and 850 μm SCUBA data from Di Francesco et al. (2008), and the IRAM 1.3 mm single-dish flux from Ward-Thompson et al. (2000). The 70 μm emission is not enhanced towards the position of C-MM3 but does peak nearby (see Section 4.1.3). We therefore take an upper limit of the 70 μm emission towards this source. The best fits to the data are from models 3011153 and 3003259,[14] giving bolometric luminosity estimates of 71 and 102 $L_\odot$, respectively, over a range of inclination angles from near edge on to ∼50 deg. These results are consistent with a previous estimate of 50 ± 10 $L_\odot$ by Maury et al. (2009) for C-MM3, again using the online SED tool Robitaille et al. (2007) and three flux measurements (*Spitzer*/MIPS 70 μm, APEX/ArTeMiS 450 μm, and IRAM 1.2 mm MAMBO data Peretto et al. 2006 see Maury et al. 2009 for more details). The remaining outflow driving source, C-MM12, is too close to AFGL-989 to unambiguously identify any IR emission associated with it. We crudely estimate a bolometric luminosity for this source assuming that the luminosity ratio between the two sources (e.g. $L_{\rm bol}^{\rm C-MM12}/L_{\rm bol}^{\rm C-MM3}$) is equal to the 1.3 mm flux density ratio. This gives an estimate of the bolometric luminosity for C-MM12 of between ∼50 and 70 $L_\odot$.

[14] http://caravan.astro.wisc.edu/protostars

4.3.3 NGC 2264-C in the context of low- and high-mass star formation studies

The correlation between outflow force and source bolometric luminosity has been previously suggested as an indication of a similar outflow driving mechanism across the low- and high-mass star-forming regimes. Fig. 12 presents previous data taken from the literature of the bolometric luminosity as a function of outflow force covering several orders of bolometric luminosity (low-mass class 0 and class I sources; van der Marel et al. 2013, Bontemps et al. 1996, intermediate-mass class 0 sources; Duarte-Cabral et al. 2013, and high-mass YSOs; Maud et al. 2015). While linear (log–log space) correlations are found between the two regimes (see Fig. 12), there is an order of magnitude scatter about these fits. The linear fit to the low-mass class I sources (Bontemps et al. 1996), when extended to the high-mass regime is found to better fit the data compared with the class 0 fit extended to the high-mass regime. While both the class 0 and class I fits have a similar gradient (Bontemps et al.

1996), the class 0 fit is, on average, offset higher by an order of magnitude compared with the class I fit.

Sources observed in the RMS sample are by selection IR-bright and thus relatively evolved compared with embedded typically younger class 0 sources. Therefore, it may not be surprising that the fit from the class I low-mass protostars has a better correlation with the high-mass outflow sources than the fit from the class 0 IR-dark sample. Moreover, as discussed in Maud et al. (2015), each high-mass outflow source, given the observed spatial resolution and distances, likely contains multiple protostars, where the luminosity of the cluster is dominated by the IR-bright RMS. Thus, the high-mass sample of outflow sources plotted in Fig. 12 have a force representing the total for the cluster, but the assumption that these are driven by the RMS, and hence have the correct bolometric luminosity, is not necessarily the case. A combination of low/intermediate-mass stars could be responsible for the observed total outflow force (e.g. Maud et al. 2015 and references therein), as observed by Klaassen et al. (2015) towards IRAS 17233−3606, and observed here in this data, where the IR-bright RMS is not found to drive an outflow.

In our SMA observations of NGC 2264-C, we find that the complex outflow emission observed in the single-dish CO observations contains two well-collimated, bipolar outflows, neither of which is driven by the IR-bright RMS. Instead, it is the likely younger, IR-dark sources C-MM3 and C-MM12 that drive the outflows in this region. The derived bolometric luminosities and outflow forces ($\dot{P}$, see Table 8) for these two sources are plotted in Fig. 12, along with an estimated upper limit for the outflow force of C-MM5/AFGL989-IRS1. We note that this is a crude estimate, calculated assuming a 20 arcsec aperture centred on C-MM5, with the ^{12}CO (2−1) emission integrated over a similar velocity range as seen in C-MM3 and C-MM12. It is stressed that this gives a very approximate limit for the outflow properties. The derived limit on the outflow force for AFGL989-IRS1 is lower than expected given its bolometric luminosity (1800 $L_{\odot}$, taken from the RMS survey), which may be a result of the more evolved nature of this source.

The estimated outflow forces for C-MM3 and C-MM12 are below what would be expected given their likely young, class 0-type nature. However, as the class 0 low-mass sample of Bontemps et al. (1996) was observed with a single-dish telescope compared with the interferometric observations performed here, even though the spatial resolution is similar (given the larger distance to NGC 2264-C, ∼738 pc) the interferometric observations will likely miss some flux. Furthermore, the outflow forces estimated for C-MM3 and C-MM12 have not been corrected for optical depth effects and are thus likely underestimated by a factor of ∼5–10 (e.g. Offner et al. 2011 Dunham et al. 2014). Maury et al. (2009) estimated a total outflow force for lobes F5 and F7 (which at the higher resolution of our SMA observations are found to be associated with C-MM12) of 4.6×10^{-4} $M_{\odot}$ km s^{-1} yr^{-1}, compared with 1.1×10^{-5} $M_{\odot}$ km s^{-1} yr^{-1} estimated here. The true value of the outflow force for C-MM12 likely lies somewhere between these two values, accounting for the spatial filtering but also the ability to separate the outflows themselves at our higher resolution.

There are still major difficulties when trying to link outflow properties between the low- and high-mass regimes; the scales probed are different, and particularly in the high-mass regime it is often not clear if a single or multiple sources are responsible for the emission. In addition, the different methods of estimating properties such as dynamical time-scales between samples make it difficult to directly compare. Richer et al. (2000) suggest the perceived correlation may not be directly related to the actual driving mechanism, as the higher masses available in the high-mass sample would provide higher values for outflow properties regardless of the underlying mechanism. This is also addressed by Maud et al. (2015), who discuss that the core mass could be the main driver of the outflow scaling relation. Taken at face value, the linear (log–log) fit between the low- and high-mass regimes does indeed suggest a correlation from low to high mass indicative of a similar formation mechanism between the regimes. However, there are significant caveats, as discussed above. Our SMA observations of NGC 2264-C emphasize the need for complementary high-resolution observations with the ability to resolve a postulated single outflow and driving core into many components, to fully probe the outflow(s) in intermediate-/high-mass star-forming regions.

5 SUMMARY

We have observed the intermediate-/high-mass star-forming region NGC 2264-C at an angular resolution of ∼3 arcsec with the SMA at 1.3 mm and provide the first interferometric observations of the outflow tracers SiO (5−4) and ^{12}CO (2−1). Of the ten 1.3 mm continuum peaks identified, four of which are new detections, only two are clearly driving bipolar outflows. The SiO (5−4) observations unambiguously reveal two high-velocity bipolar outflows, driven by C-MM3 and C-MM12. High-velocity emission from SO, ^{12}CO, and H_2CO, along with lower velocity emission from CH_3OH, also traces both outflows. Comparing our SMA data to our JCMT SiO (8−7) observations, we find that SiO (8−7) is detected only towards these two bipolar outflows with the JCMT. In the lower resolution JCMT observations, the outflow driving sources are ambiguous. Thus, the combination of these observations emphasizes the power of high-resolution, multiline observations to remove ambiguity in identifying outflow driving sources.

We find a clear evolutionary differentiation among the continuum sources present in this cluster. Comparison of the molecular chemistry and of the mid- and far-IR, millimetre, submillimetre, and radio emission reveals that it is the likely youngest, mm brightest sources, C-MM3, and C-MM12, that are driving the dominant bipolar outflows. Both of these cores are IR-dark and molecular line weak and have no detected centimetre-λ radio emission, indicating that they are likely at a very early stage of evolution. In contrast, the IR-bright, most evolved source in the region, the RMS AFGL 989-IRS1, does not drive a molecular outflow. However, the wind from this source (Bunn et al. 1995) is likely driving a low-density cavity (Schreyer et al. 2003) that may be responsible for the molecular line rich 'ridge' feature we observe, including its class I CH_3OH maser emission.

ACKNOWLEDGEMENTS

We thank the anonymous referee for helpful comments that have improved the content and overall clarity of this manuscript. CJC acknowledges support from the STFC (grant number ST/M001296/1). CJC was partially supported during this work by a National Science Foundation Astronomy and Astrophysics Postdoctoral Fellowship under award AST-1003134. The authors are very grateful to N. Peretto for providing the reduced PdBI N_2H^+ (1−0) integrated intensity maps that were published in Peretto et al. (2007). This research made use of APLPY, an open-source plotting package for PYTHON hosted at http://aplpy.github.com; astrodendro, a dendrogram plotting routine for PYTHON hosted at http://www.dendrograms.org/ and the Splatalogue molecular data base (http:/splatalogue.net/).

REFERENCES

Allen D. A., 1972, ApJ, 172, L55
Araya E., Hofner P., Kurtz S., Bronfman L., DeDeo S., 2005, ApJS, 157, 279
Astropy Collaboration et al., 2013, A&A, 558, A33
Battersby C. et al., 2011, A&A, 535, A128
Bell T. A., Cernicharo J., Viti S., Marcelino N., Palau A., Esplugues G. B., Tercero B., 2014, A&A, 564, A114
Beuther H., Schilke P., Sridharan T., Menten K., Walmsley C., Wyrowski F., 2002, A&A, 383, 892
Beuther H. et al., 2004, ApJ, 616, L23
Beuther H., Shepherd D., 2005, in Kumar M., Tafalla M., Caselli P., eds, Cores to Clusters: Star Formation with Next Generation Telescopes. Springer-Verlag, New York, p. 105
Bontemps S., Andre P., Terebey S., Cabrit S., 1996, A&A, 311, 858
Brogan C. L., Hunter T. R., Cyganowski C. J., Indebetouw R., Beuther H., Menten K. M., Thorwirth S., 2009, ApJ, 707, 1
Buckle J. V. et al., 2009, MNRAS, 399, 1026
Bunn J. C., Hoare M. G., Drew J. E., 1995, MNRAS, 272, 346
Cabrit S., Bertout C., 1992, A&A, 261, 274
Carrasco-González C., Rodríguez L., Anglada G., Martí J., Torrelles J., Osorio M., 2010, Science, 330, 1209
Cesaroni R., Galli D., Neri R., Walmsley C. M., 2014, A&A, 566, A73
Codella C., Beltrán M., Cesaroni R., Moscadelli L., Neri R., Vasta M., Zhang Q., 2013, A&A, 550, A81
Codella C., Maury A. J., Gueth F., Maret S., Belloche A., Cabrit S., André P., 2014, A&A, 563, L3
Csengeri T., Bontemps S., Schneider N., Motte F., Gueth F., Hora J. L., 2011, ApJ, 740, L5
Cyganowski C. J., Brogan C. L., Hunter T. R., Churchwell E., 2009, ApJ, 702, 1615
Cyganowski C. J., Brogan C. L., Hunter T. R., Churchwell E., Zhang Q., 2011, ApJ, 729, 124
Cyganowski C., Brogan C., Hunter T., Zhang Q., Friesen R., Indebetouw R., Chandler C., 2012, ApJ, 760, L20
Davies B., Hoare M. G., Lumsden S. L., Hosokawa T., Oudmaijer R. D., Urquhart J. S., Mottram J. C., Stead J., 2011, MNRAS, 416, 972
Di Francesco J., Johnstone D., Kirk H., MacKenzie T., Ledwosinska E., 2008, ApJS, 175, 277
Duarte-Cabral A., Bontemps S., Motte F., Hennemann M., Schneider N., André P., 2013, A&A, 558, A125
Dunham M. M., Arce H. G., Mardones D., Lee J.-E., Matthews B. C., Stutz A. M., Williams J. P., 2014, ApJ, 783, 29
Fish V. L., Muehlbrad T. C., Pratap P., Sjouwerman L. O., Strelnitski V., Pihlström Y. M., Bourke T. L., 2011, ApJ, 729, 14
Flaccomio E., Micela G., Sciortino S., 2006, A&A, 455, 903
Fontani F., Zhang Q., Caselli P., Bourke T. L., 2009, A&A, 499, 233
Frerking M. A., Langer W. D., Wilson R. W., 1982, ApJ, 262, 590
Galván-Madrid R., Zhang Q., Keto E., Ho P., Zapata L., Rodríguez L., Pineda J., Vázquez-Semadeni E., 2010, ApJ, 725, 17
Gibb A. G., Richer J. S., Chandler C. J., Davis C. J., 2004, ApJ, 603, 198
Gibb A., Davis C., Moore T., 2007, MNRAS, 382, 1213
Goldsmith P. F., Langer W. D., 1999, ApJ, 517, 209
Gómez-Ruiz A. I., Hirano N., Leurini S., Liu S.-Y., 2013, A&A, 558, A94
Grellmann R., Ratzka T., Kraus S., Linz H., Preibisch T., Weigelt G., 2011, A&A, 532, A109
Guillet V., Jones A. P., Pineau Des Forêts G., 2009, A&A, 497, 145
Gusdorf A., Cabrit S., Flower D. R., Pineau Des Forêts G., 2008a, A&A, 482, 809
Gusdorf A., Pineau Des Forêts G., Cabrit S., Flower D. R., 2008b, A&A, 490, 695
Haschick A. D., Menten K. M., Baan W. A., 1990, ApJ, 354, 556
Hunter T. R., Brogan C. L., Indebetouw R., Cyganowski C. J., 2008, ApJ, 680, 1271
Hunter T. R., Brogan C. L., Cyganowski C. J., Young K. H., 2014, ApJ, 788, 187
Immer K., Galván-Madrid R., König C., Liu H. B., Menten K. M., 2014, A&A, 572, A63
Kamezaki T. et al., 2014, ApJS, 211, 18
Kim K.-T., Kurtz S., 2006, ApJ, 643, 978
Klaassen P. D., Plume R., Ouyed R., von Benda-Beckmann A. M., Di Francesco J., 2006, ApJ, 648, 1079
Klaassen P., Testi L., Beuther H., 2012, A&A, 538, A140
Klaassen P. D., Johnston K. G., Leurini S., Zapata L. A., 2015, A&A, 575, A54
Kurtz S., Hofner P., Álvarez C. V., 2004, ApJS, 155, 149
Lada C. J., Lada E. A., 2003, ARA&A, 41, 57
Lee C.-F., Hasegawa T. I., Hirano N., Palau A., Shang H., Ho P. T. P., Zhang Q., 2010, ApJ, 713, 731
Leurini S., Codella C., Gusdorf A., Zapata L., Gómez-Ruiz A., Testi L., Pillai T., 2013, A&A, 554, A35
Leurini S., Codella C., López-Sepulcre A., Gusdorf A., Csengeri T., Anderl S., 2014, A&A, 570, A49
López-Sepulcre A. et al., 2011, A&A, 526, L2
Loren R. B., Mundy L. G., 1984, ApJ, 286, 232
Lumsden S. L., Hoare M. G., Urquhart J. S., Oudmaijer R. D., Davies B., Mottram J. C., Cooper H. D. B., Moore T. J. T., 2013, ApJS, 208, 11
Mangum J. G., Shirley Y. L., 2015, PASP, 127, 266
Maud L. T., Moore T. J. T., Lumsden S. L., Mottram J. C., Urquhart J. S., Hoare M. G., 2015, MNRAS, 453, 645
Maury A., André P., Li Z.-Y., 2009, A&A, 499, 175
Müller H. S. P., Schlöder F., Stutzki J., Winnewisser G., 2005, J. Mol. Struct., 742, 215
Nakano M., Sugitani K., Morita K., 2003, PASJ, 55, 1
Offner S. S. R., Lee E. J., Goodman A. A., Arce H., 2011, ApJ, 743, 91
Ossenkopf V., Henning T., 1994, A&A, 291, 943
Peretto N., André P., Belloche A., 2006, A&A, 445, 979
Peretto N., Hennebelle P., André P., 2007, A&A, 464, 983
Pilbratt G. L. et al., 2010, A&A, 518, L1
Plambeck R. L., Menten K. M., 1990, ApJ, 364, 555
Poglitsch A., Waelkens C., Geis N., Feuchtgruber H., Vandenbussche B., Rodriguez L., Krause O., Renotte E., 2010, A&A, 518, L2
Qiu K., Zhang Q., 2009, ApJ, 702, L66
Qiu K., Zhang Q., Wu J., Chen H.-R., 2009, ApJ, 696, 66
Reipurth B., Rodríguez L. F., Anglada G., Bally J., 2004, AJ, 127, 1736
Richer J., Shepherd D., Cabrit S., Bachiller R., Churchwell E., 2000, Protostars and Planets IV. Univ. Arizona Press, Tucson, AZ, 867
Rieke G. H., Young E. T., Engelbracht C. W., Kelly D. M., Low F. J., Haller E. E., Beeman J. W., Gordon K. D., 2004, ApJS, 154, 25
Robitaille T. P., Whitney B. A., Indebetouw R., Wood K., 2007, ApJS, 169, 328
Rosolowsky E. W., Pineda J. E., Kauffmann J., Goodman A. A., 2008, ApJ, 679, 1338
Sakai T., Sakai N., Hirota T., Yamamoto S., 2010, ApJ, 714, 1658
Sánchez-Monge Á., López-Sepulcre A., Cesaroni R., Walmsley C. M., Codella C., Beltrán M. T., Pestalozzi M., Molinari S., 2013, A&A, 557, A94
Santiago-García J., Tafalla M., Johnstone D., Bachiller R., 2009, A&A, 495, 169
Saruwatari O., Sakai N., Liu S.-Y., Su Y.-N., Sakai T., Yamamoto S., 2011, ApJ, 729, 147
Sault R. J., Teuben P. J., Wright M. C. H., 1995, in Shaw R. A., Payne H. E., Hayes J. J. E., eds, ASP Conf. Ser. Vol. 77, Astronomical Data Analysis Software and Systems IV. Astron. Soc. Pac., San Francisco, p. 433
Schilke P., Walmsley C. M., Pineau des Forets G., Flower D. R., 1997, A&A, 321, 293
Schreyer K., Helmich F., van Dishoeck E., Henning T., 1997, A&A, 326, 347
Schreyer K., Stecklum B., Linz H., Henning T., 2003, ApJ, 599, 335
Shepherd D. S., Churchwell E., 1996, ApJ, 472, 225
Skrutskie M. F. et al., 2006, AJ, 131, 1163
Slysh V. I., Kalenskii S. V., 2009, Astron. Rep., 53, 519
Slysh V. I., Kalenskiĭ S. V., Val'tts I. E., 2002, Astron. Rep., 46, 49

Tafalla M., Santiago-García J., Hacar A., Bachiller R., 2010, A&A, 522, A91
Vaidya B., Fendt C., Beuther H., Porth O., 2011, ApJ, 742, 56
van der Marel N., Kristensen L. E., Visser R., Mottram J. C., Yıldız U. A., van Dishoeck E. F., 2013, A&A, 556, A76
Voronkov M. A., Caswell J. L., Britton T. R., Green J. A., Sobolev A. M., Ellingsen S. P., 2010, MNRAS, 408, 133
Voronkov M. A., Caswell J. L., Ellingsen S. P., Green J. A., Breen S. L., 2014, MNRAS, 439, 2584
Wang K. et al., 2014, MNRAS, 439, 3275
Ward-Thompson D., Zylka R., Mezger P., Sievers A., 2000, A&A, 355, 1122
Wu Y., Wei Y., Zhao M., Shi Y., Yu W., Qin S., Huang M., 2004, A&A, 426, 503
Zhang Q., Ho P. T. P., Ohashi N., 1998, ApJ, 494, 636
Zhang Q., Hunter T. R., Brand J., Sridharan T. K., Cesaroni R., Molinari S., Wang J., Kramer M., 2005, ApJ, 625, 864
Zhang Q., Hunter T. R., Beuther H., Sridharan T. K., Liu S.-Y., Su Y.-N., Chen H.-R., Chen Y., 2007, ApJ, 658, 1152

This paper has been typeset from a TEX/LATEX file prepared by the author.